SEDIMENTOLOGY the journal of the International Association of Sedimentologists

Sedimentology (2025) doi: 10.1111/sed.70032

Three-dimensional gravity current interactions with oblique slopes: Deflection, reflection and combined-flow behaviours

RU WANG, JEFF PEAKALL, DAVID M. HODGSON, ED KEAVNEY, HELENA C. BROWN and GARETH M. KEEVIL
School of Earth & Environment, University of Leeds, Leeds LS2 9JT, UK (E-mail: earrwa@leeds.ac.uk)
(E-mail: 13269878303@163.com)

Associate Editor – Lawrence Amy

ABSTRACT

Gravity currents interacting with planar slopes have been thought to always 'reflect' a component of flow orthogonal to the slope irrespective of the flow incidence angle. Incoming flows are argued to undergo gravitational collapse, and generate internal waves, that propagate perpendicular to the bounding slope. These processes have been used to explain the widespread observation of palaeocurrents from sole marks at high angles to those in the associated ripple division. This paradigm for gravity current interactions with planar slopes has stood for more than three decades. Herein, these ideas are tested using three-dimensional low-density saline currents interacting with (but not overtopping) planar slopes of varying gradients, at a range of incidence angles. Fifteen new experiments show that the dominant flow process transitions from divergence-, through reflection- to deflection-dominated as the flow incidence angle decreases from 90° to 15° and the slope gradient increases from 20° to 40°. Multidirectional combined flows are documented above topographic slopes, varying as a function of location on a single slope, and the orientation and gradient of the slope. However, discrete internal waves are not observed, likely due to the spatial and temporal variability of flows on the slope. These findings challenge the paradigm of flow deflection and reflection in the existing model; there is not always a component of 'reflected' flow orthogonal to the planar slope. A new process model for flow-planar-slope interactions is presented. Flows broadly parallel to topographic slopes lead to up-slope and down-slope flow oscillations orthogonal to the bounding slope, providing new mechanics for the observation of high-angle variation between sole marks and ripple derived palaeocurrents in elongate basin-fills. Results also provide insights into the spatial distribution of distinctive combined-flow bedforms, which are most applicable to settings where flows interact with high-relief intrabasinal topography and/or basin margins.

Keywords Combined flow, flow deflection, flow reflection, incidence angle, slope gradient, three-dimensional turbidity current, topographic slope, velocity pulsing.

INTRODUCTION

Turbidity currents are subaqueous gravity-driven turbulent flows that serve as important mechanisms for the transfer of large volumes of clastic sediments from continents to the deep oceans (e.g. Kuenen & Migliorini, 1950; Dzulynski *et al.*, 1959; Sestini, 1970; Normark *et al.*, 1993; Kneller & Buckee, 2000). Seafloor topography influences turbidity current behaviour, and therefore, the distribution and nature of their deposits. The interplay of several factors needs

© 2025 The Author(s). *Sedimentology* published by John Wiley & Sons Ltd on behalf of International Association of Sedimentologists.
This is an open access article under the terms of the Creative Commons Attribution License, which permits use, distribution and reproduction in any medium, provided the original work is properly cited.

to be considered in the interaction of turbidity currents and topography (e.g. Kneller *et al.*, 1991, 1997; Edwards *et al.*, 1994; Amy *et al.*, 2004; Brunt *et al.*, 2004; Patacci *et al.*, 2015; Howlett *et al.*, 2019; Reece *et al.*, 2024, 2025 and references therein), including flow duration (surge versus sustained or quasi-steady flow), the relative volume of the flow versus the size of the basin ('flow confinement', hereafter; *sensu* Tőkés & Patacci, 2018; cf. Pickering & Hiscott, 1985; Southern *et al.*, 2015), and the configuration of the containing topography (e.g. slope gradient, orientation, geometry and elevation; 'topographic containment', hereafter). When the volume of the flow is small relative to the size of the basin, the flow can expand in the basin freely, which is referred to as unconfined flow in this work. In the presence of seafloor topography, flows can be reflected, deflected and/or constricted depending on the configuration of the containing topography and the flow properties (e.g. thickness, viscosity and velocity).

A better understanding of the complicated interactions between turbidity currents and seafloor topography, and the links to depositional character, is critical in a wide range of situations. For example, palaeogeographical reconstruction of ancient deep-water basins (e.g. Sinclair, 1994; Lomas & Joseph, 2004; Bell *et al.*, 2018), hydrocarbon or CO_2 reservoir characterization in the subsurface (e.g. McCaffrey & Kneller, 2001; Chadwick *et al.*, 2004; Bakke *et al.*, 2013; Lloyd *et al.*, 2021), modern mass-flow geohazard assessment in deep-water environments (e.g. Bruschi *et al.*, 2006; Carter *et al.*, 2014), prediction of plastic litter and other pollutant distribution in the deep sea (e.g. Haward, 2018; Kane *et al.*, 2020) and de-risking management of sedimentation in modern human-made water reservoirs (e.g. Wei *et al.*, 2013).

The opaque nature of natural turbidity currents and limited field instrumental measurements have restricted the understanding of the interaction between turbidity currents and containing topography. Advances have been made mainly through scaled-down physical experiments (e.g. Pantin & Leeder, 1987; Muck & Underwood, 1990; Kneller *et al.*, 1991; Alexander & Morris, 1994; Edwards *et al.*, 1994; Amy *et al.*, 2004; Patacci *et al.*, 2015; Soutter *et al.*, 2021; Reece *et al.*, 2024, 2025), numerical modelling (e.g. Athmer *et al.*, 2010; Howlett *et al.*, 2019) and facies analysis of exhumed systems (e.g. Kneller *et al.*, 1991; Haughton, 2000; Tinterri *et al.*, 2016, 2022).

The existing paradigm for sediment gravity flow interaction with topography is that there is a component of the return flow that is always orthogonal to the planar slope irrespective of the flow incidence angle (Kneller *et al.*, 1991; Kneller, 1995; Kneller & McCaffrey, 1999; cf. high angles to orthogonal of Pickering *et al.*, 1992). This orthogonal return flow down the slope was postulated as due to gravitational collapse, and termed 'reflection' by Kneller *et al.* (1991). These gravitational collapses are linked to either bores (moving hydraulic jumps), or the generation of internal waves, or solitons, propagating perpendicular to the bounding slope, at the flow-ambient water interface (Pantin & Leeder, 1987; Kneller *et al.*, 1991; Edwards *et al.*, 1994). These propagating internal waves, or solitons, provide an explanation for the frequent observation of palaeocurrents from sole marks at high angles to those in the associated ripple division (Kneller *et al.*, 1991; Smith & Anketell, 1992; Kneller, 1995). Field-based research also reinforced this model, with orthogonal 'reflection' argued to be produced from all incidence angles, linked to flow pulses where there were periods dominated by downslope flow collapse (Kneller & McCaffrey, 1999).

Importantly, the previous experimental studies focusing on the interactions between gravity currents and planar topographic slopes were conducted either in narrow 2D flume tanks (e.g. Edwards *et al.*, 1994; Amy *et al.*, 2004; Patacci *et al.*, 2015), in small ($1\,m^2$ planform) 3D tanks (Kneller *et al.*, 1991; Kneller, 1995) or in large 3D tanks with low-relief topographic configurations that are surmountable by the inlet flows (Soutter *et al.*, 2021). In these experiments, they notably used high-density flows. In contrast, recent work in large 3D tanks using low-density saline currents and high-relief topography has shown that complex unconfined gravity flow behaviour can be generated even in simple configurations with orthogonal, planar slopes (Keavney *et al.*, 2025). The Keavney *et al.* (2025) study thus indicates that there remains much to learn. In particular, the behaviour of 3D unconfined gravity currents that interact with different planar slope configurations has not been investigated. Outcrop-based models of confined and contained turbidites are derived from purely theoretical analysis with limited 3D constraints (e.g. Kneller & McCaffrey, 1999; Hodgson & Haughton, 2004), or from linking to existing 2D flume experimental data (e.g. Tinterri *et al.*, 2016, 2022). Therefore, their significance in

© 2025 The Author(s). *Sedimentology* published by John Wiley & Sons Ltd on behalf of International Association of Sedimentologists, *Sedimentology*

13653091, 0, Downloaded from https://onlinelibrary.wiley.com/doi/10.1111/sed.70032 by Schweizerische Akademie Der, Wiley Online Library on [20/07/2025]. See the Terms and Conditions (https://onlinelibrary.wiley.com/terms-and-conditions) on Wiley Online Library for rules of use; OA articles are governed by the applicable Creative Commons License

understanding the temporal and spatial variability in the dynamics of flow interactions with planar topography interactions is limited.

Combined flows and the formation of hummock-like or sigmoidal bedforms in deep-water systems have previously been linked to the interaction of turbidity currents with topography and the superposition of a unidirectional parental turbidity current with an oscillatory component due to reflection against a topographic slope (Kneller *et al.*, 1991; Edwards *et al.*, 1994; Tinterri, 2011; Patacci *et al.*, 2015; Tinterri *et al.*, 2016, 2022), largely based on the observations from 2D or qualitative 3D reflected density current experiments (e.g. Kneller *et al.*, 1991; Edwards *et al.*, 1994). The nature and generation mechanisms of the internal waves in these models of combined flow bedforms are not specified; however, we note that internal waves can be formed as: (i) reflected bores translating into internal waves as described earlier; (ii) a product of flow instabilities such as Kelvin–Helmholtz instabilities propagating along the steepest density contrast interface (e.g. Patacci *et al.*, 2015); or (iii) internal to the flow around the position of the velocity maximum (e.g. Marshall *et al.*, 2021, 2023). Based on experimental observations of 3D density currents interacting with an orthogonal planar slope, Keavney *et al.* (2025) propose a new mechanism for the generation of combined flows on planar slopes, with the absence of internal waves. However, whether the new mechanism holds in cases where 3D density currents interact with an oblique planar topographic slope has not been investigated experimentally.

In this work, a series of generic Froude-scaled 3D physical experiments were conducted using sustained, 3D saline density currents, where the flow was partially contained by a rigid planar slope. The flows did not overtop the barrier but were able to flow downstream around the slope. Here, dissolved salt acts as a surrogate for fine mud in suspension that does not easily settle out, moves in bypass mode and therefore flows used in this work can be considered to model low-density turbidity currents (Sequeiros *et al.*, 2010). The overall aim of this work was to systematically investigate the effects of different configurations of planar topographic slopes on the flow behaviour, including the incidence angle of the flow onto the slope and slope gradient. To achieve this, the following three objectives are undertaken: (i) to investigate the influence of containing topography on the general flow behaviour, including flow decoupling and stripping, lateral flow expansion on the slope surface and the relative strength between flow deflection versus reflection; (ii) to explore the effect of containing topography on the temporal near-bed velocity pulsation patterns, a property that is crucial for sediment erosion and deposition; and (iii) to assess the effect of containing topography on the temporal variability of near-bed flow directions.

The results are subsequently discussed considering their implications for the development of new models of flow interactions with planar topography, and spatial distribution of complex, multidirectional combined flows in deep-water settings. Finally, these findings are used to provide insights into the spatial distribution of distinctive combined-flow bedforms on topographic slopes. Notably, the findings of this work are most applicable to deep-water basins where the flow interacts with high-relief intrabasinal topography and/or basin margins with a quasi-steady low-density input flow source. For example, syn- and early post-rift (e.g. Ravnås & Steel, 1997; Cullen *et al.*, 2020) or oblique-slip (Hodgson & Haughton, 2004; Baudouy *et al.*, 2021) settings where fault scarps have a pronounced seafloor expression.

METHODOLOGY

Experimental design

Experiments were conducted in the Sorby Environmental Fluid Dynamics Laboratory, University of Leeds. The basic set up of the experiments follows Keavney *et al.* (2025). The flume tank used is 10 m long, 2.5 m wide and 1 m deep, with a flat basin floor (Fig. 1A). A 1.8 m long straight-sided input channel section (0.26 m wide and 0.5 m deep) with an embedded 1.18 m long diffuser pipe (0.15 m diameter) placed on the central experimental platform was centred in the upstream end of the main tank. The saline density current entered the main tank through the diffuser pipe first and then flowed through the straight channel before debouching into the main tank. The inlet flow was confined to the straight-sided channel. For simplicity, the straight channel was set flat, that is, with 0° slope angle. The diffuser pipe prevented the development of a jet flow being directed straight down the tank. Before each experiment, the

© 2025 The Author(s). *Sedimentology* published by John Wiley & Sons Ltd on behalf of International Association of Sedimentologists, *Sedimentology*

13653091, 0, Downloaded from https://onlinelibrary.wiley.com/doi/10.1111/sed.70032 by Schweizerische Akademie Der, Wiley Online Library on [20/07/2025]. See the Terms and Conditions (https://onlinelibrary.wiley.com/terms-and-conditions) on Wiley Online Library for rules of use; OA articles are governed by the applicable Creative Commons License

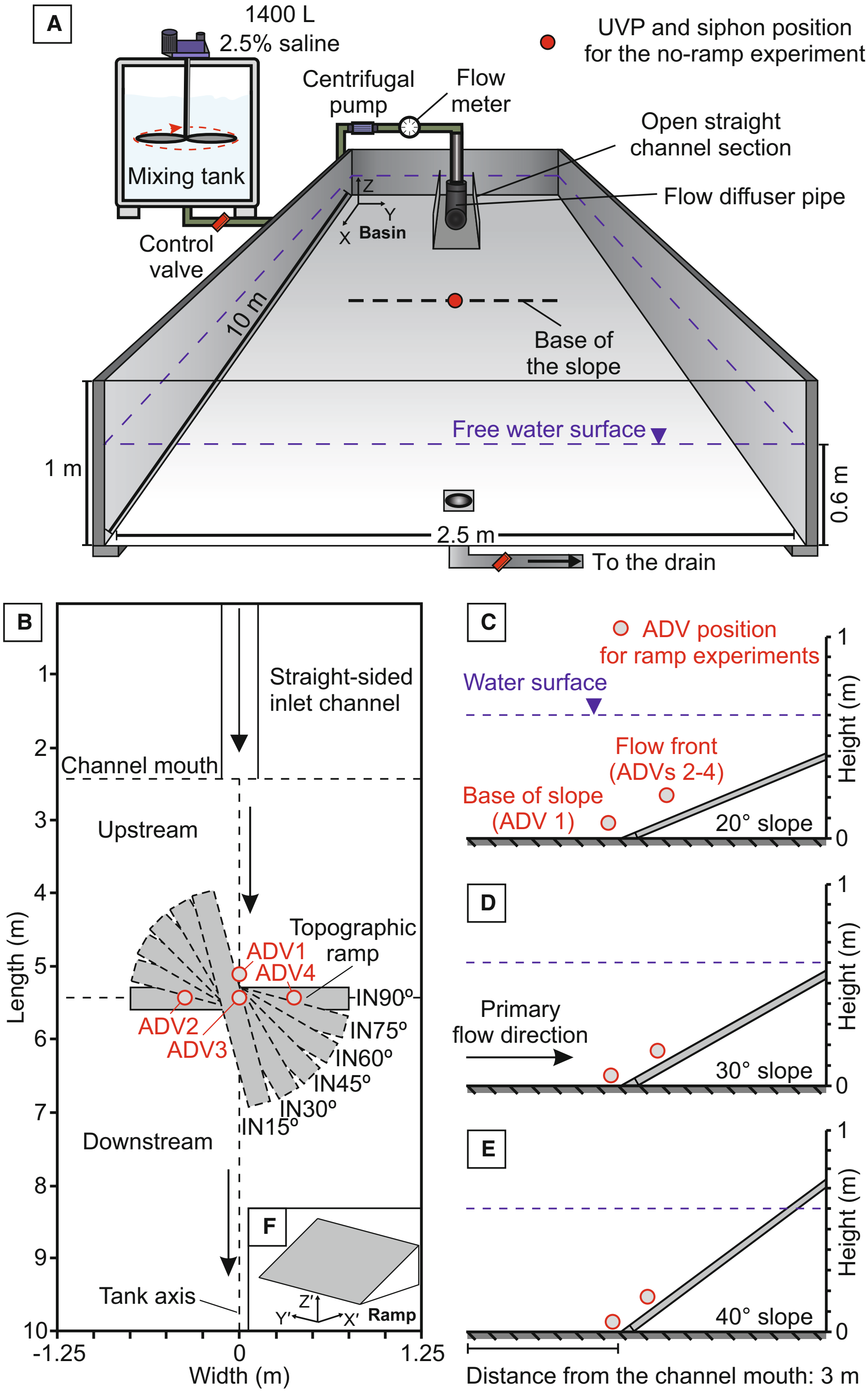

Fig. 1. (A) Schematic sketch of the experimental facility. Note that the base of the containing topographic ramp is indicated as a black dashed line. The position of the Ultrasonic Velocity Profiler (UVP) and siphoning system for the no-ramp experiment is also indicated. (B–E) Topographic configurations of the ramp experiments with different combinations of slope gradients and incidence angles relative to the incoming flow. (B) Ramp with different incidence angles relative to the incoming flow shown in a plan view. The left side and right side of the tank are relative to the incoming flow. (C–E) Ramp with different slope gradients shown in a side view. Measuring localities of the four Acoustic Doppler Velocimeters (ADVs) for each ramp experiment are illustrated (ADVs 1–4). Two sets of Cartesian coordinate systems are adopted relative to the basin floor (A) or to the ramp (F).

13653091, 0, Downloaded from https://onlinelibrary.wiley.com/doi/10.1111/sed.70032 by Schweizerische Akademie Der, Wiley Online Library on [20/07/2025]. See the Terms and Conditions (https://onlinelibrary.wiley.com/terms-and-conditions) on Wiley Online Library for rules of use; OA articles are governed by the applicable Creative Commons License

main tank was filled with fresh tap water to 0.6 m deep. A saline solution of excess density 2.5% (1025 kg m^{-3}) was prepared in a 2 m^3 mixing tank with an electric rotary mixer utilized to ensure a uniform salt concentration. The saline density current was subsequently pumped into the main tank at a constant discharge rate of 3.6 L s^{-1} (Table 1). Water density and temperature were measured using a portable densimeter (DMA35, Anton Parr, Graz, Austria; resolution of 0.1 kg m^{-3} and 0.1°C, respectively) in both the main tank and the mixing tank before each experimental run (Table 1). The discharge rate was controlled by an inverter-governed centrifugal pump and monitored in real time by an electromagnetic flowmeter (Fig. 1A). Each experiment started with the release of the flow from the mixing tank to the main tank.

The first experimental configuration was run without any basin-floor topography ('no-ramp experiment' hereafter; see details in Keavney *et al.*, 2025) and served as a base-case experiment. Fifteen new ramp experiments were conducted with a non-erodible, smooth, planar ramp (1.5 m wide and 1.2 m long) placed on the base of the flume tank, with three orthogonal-flow-ramp experiments from Keavney *et al.* (2025) for comparison. The dimensions of the planar slope were chosen to better simulate the interaction between gravity currents and intrabasinal topography. The ramp had a tapered leading edge at the foot abutting the basin floor, which minimized any step discontinuity, but the lateral edges of the ramp were not tapered. Flow around/off these lateral edges experiences a sudden drop in elevation and increase in velocity. However, the instabilities of this phenomenon were observed to largely propagate basinward with limited influence on the flow dynamics on the slope surface (the affected area is within 3 cm from the lateral edge, *ca* 2% of the slope width; Videos 1–4 in this study and Videos 2–4 in Keavney *et al.*, 2025). The leading edge at the foot of the ramp was placed 3 m downstream from the channel mouth (black dashed line in Fig. 1A), with its centrepoint located on the channel-basin centreline (red circle in Fig. 1A). This position was chosen as the density current had lost the effects of upstream confinement and was relatively unconfined (see *Gravity current evolution in the unconfined experiment* subsection). In these ramp experiments, the slope gradient (S) and incidence angle (IN) were systematically varied. Each experiment (Table 1) considers a different combination of incidence angle relative to the incoming flow (i.e. 90°, 75°, 60°, 45°, 30° and 15°; Fig. 1B) and ramp slope gradient (i.e. 20°, 30° and 40°; Fig. 1C–E). The maximum barrier height in these topographic configurations is 0.410 m, 0.585 m and 0.760 m, respectively, and was tested to be able to fully contain the flow vertically, that is, the density current did not surmount the topography.

The choice of ramp slope gradients used in this work is informed by previous similar experimental models utilizing slope angles ranging from 20° to 30° (e.g. Muck & Underwood, 1990; Kneller *et al.*, 1991; Kneller, 1995; Soutter *et al.*, 2021), topographic slopes in natural systems and constrained by the initial water depth of the experimental basin design in this work (Keavney *et al.*, 2025). Locally steep topography exists in natural deep-water settings, including those related to mass transport deposits (e.g. Armitage *et al.*, 2009; Martínez-Doñate *et al.*, 2021; Allen *et al.*, 2022), folds and faults (e.g. Haughton, 2000; Hodgson & Haughton, 2004; Cullen *et al.*, 2020), salt and mud diapirism (e.g. Kneller & McCaffrey, 1995; Toniolo *et al.*, 2006; Cumberpatch *et al.*, 2021; Howlett *et al.*, 2021) and volcanic seamounts (e.g. Seabrook *et al.*, 2023). Additionally, in ancient outcrop examples from the Gres d'Annot, SE France, the basin margin slope angle is estimated to range from 10° to 30° prior to compaction, calculated from the pinchout rate of the stratigraphic section onto the slope (Sinclair, 1994; Hilton & Pickering, 1998; Kneller & McCaffrey, 1999; Joseph *et al.*, 2000; Puigdefàbregas *et al.*, 2004; Smith & Joseph, 2004; Tomasso & Sinclair, 2004; Soutter *et al.*, 2019). Nevertheless, it is recognized that gentler topographic slopes less than 10° are common in many deep-water basins (e.g. Bakke *et al.*, 2013; Spychala *et al.*, 2017). Slope gradients lower than 20° were herein, however, not pursued using the current experimental setting as the flow would partially surmount the topographic slope. The implications of this experimental work for lower angle slopes will be discussed later.

Experimental data collection

No-ramp experiment

In the no-ramp experiment, three repeats were run using near identical initial conditions but for different purposes (Fig. 1A): (i) flow visualization with an overhead camera; (ii) velocity

© 2025 The Author(s). *Sedimentology* published by John Wiley & Sons Ltd on behalf of International Association of Sedimentologists, *Sedimentology*

13653091, 0, Downloaded from https://onlinelibrary.wiley.com/doi/10.1111/sed.70032 by Schweizerische Akademie Der, Wiley Online Library on [20/07/2025]. See the Terms and Conditions (https://onlinelibrary.wiley.com/terms-and-conditions) on Wiley Online Library for rules of use; OA articles are governed by the applicable Creative Commons License

Table 1. Experimental parameters. T_{inflow} water temperature in the mixing tank. T_{maintank} water temperature in the main tank. Note that three repeats were conducted for both the no-ramp experiment and each ramp experiment due to experimental constraints. For simplicity, the syntax of the ramp experiments is abbreviated as slope angle (S) in degrees followed by incidence angle (IN) in degrees, shown in the first column of the table.

Experiment	Slope angle (°)	Incidence angle (°)	Data collected	Mean flow rate (L s^{-1})	T_{inflow} (°C)	T_{maintank} (°C)	Inlet flow density (kg m^{-3})
No-ramp	N/A	N/A	Flow visualization; a UVP and density siphoning system positioned at 3 m downstream of the channel mouth along the channel-basin centreline	3.61, 3.60, 3.60	13.2, 7.5, 6.0	13.8, 7.9, 6.8	1025, 1025, 1025
S20°IN90°	20	90	Flow visualization; four ADVs (one positioned at the base of the slope along the channel-basin centreline and the other three at the flow front positions above the slope surface)	3.60, 3.61, 3.60	9.3, 9.6, 9.8	9.9, 10.0, 9.7	1025.1, 1025, 1024.9
S20°IN75°	20	75		3.59, 3.61, 3.60	20.9, 20.2, 20.0	21, 20.4, 20.7	1025, 1024.6, 1025
S20°IN60°	20	60		3.59, 3.60, 3.59	19.8, 19.4, 19.0	20, 19.6, 19.6	1025, 1024.6, 1024.9
S20°IN45°	20	45		3.59, 3.59, 3.59	18.5, 18.4, 18.4	19.0, 18.7, 18.7	1025.2, 1024.8, 1025
S20°IN30°	20	30		3.59, 3.60, 3.60	18.4, 18.8, 18.5	19.1, 19.0, 19.0	1025, 1025.2, 1024.8
S20°IN15°	20	15		3.60, 3.59, 3.59	18.9, 19.0, 19.2	19.4, 19.4, 19.6	1024.8, 1024.9, 1025
S30°IN90°	30	90		3.59, 3.59, 3.60	7.4, 8.0, 7.9	7.7, 7.8, 8.3	1024.9, 1024.9, 1025
S30°IN75°	30	75		3.60, 3.59, 3.59	19.2, 18.9, 19.9	19.5, 19.2, 20.1	1025.4, 1024.5, 1024.5
S30°IN60°	30	60		3.60, 3.60, 3.60	19.8, 19.8, 20.8	20.2, 21.1, 21.1	1025.2, 1024.8, 1025
S30°IN45°	30	45		3.59, 3.60, 3.59	20.1, 20.1, 20.2	20.8, 20.8, 20.6	1025, 1024.8, 1024.5
S30°IN30°	30	30		3.60, 3.60, 3.60	20.0, 19.4, 19.6	20.4, 19.8, 20.0	1024.9, 1025, 1024.6
S30°IN15°	30	15		3.59, 3.59, 3.60	20.0, 19.8, 19.8	20.4, 20.2, 20.1	1024.7, 1025, 1024.9
S40°IN90°	40	90		3.58, 3.59, 3.59	9.6, 9.7, 9.8	10.1, 10.0 10.2	1025, 1024.9, 1025
S40°IN75°	40	75		3.60, 3.60, 3.62	19.4, 19.1, 19.3	19.8, 19.4, 19.6	1024.3, 1025.3, 1025.3
S40°IN60°	40	60		3.60, 3.60, 3.60	19.9, 19.6, 19.7	20.0, 20.0, 20.1	1024.9, 1025.3, 1025.3
S40°IN45°	40	45		3.59, 3.60, 3.59	16.9, 16.9, 16.7	17.2, 17.0, 17.0	1024.9, 1025, 1025
S40°IN30°	40	30		3.59, 3.59, 3.60	18.8, 17.8, 17.8	19.1, 18.1, 18.2	1024.9, 1025.3, 1025
S40°IN15°	40	15		3.60, 3.59, 3.60	18.7, 18.7, 17.8	19.0, 19.1, 18.2	1025.3, 1025, 1025

© 2025 The Author(s). *Sedimentology* published by John Wiley & Sons Ltd on behalf of
International Association of Sedimentologists, *Sedimentology*

13653091, 0, Downloaded from https://onlinelibrary.wiley.com/doi/10.1111/sed.70032 by Schweizerische Akademie Der, Wiley Online Library on [20/07/2025]. See the Terms and Conditions (https://onlinelibrary.wiley.com/terms-and-conditions) on Wiley Online Library for rules of use; OA articles are governed by the applicable Creative Commons License

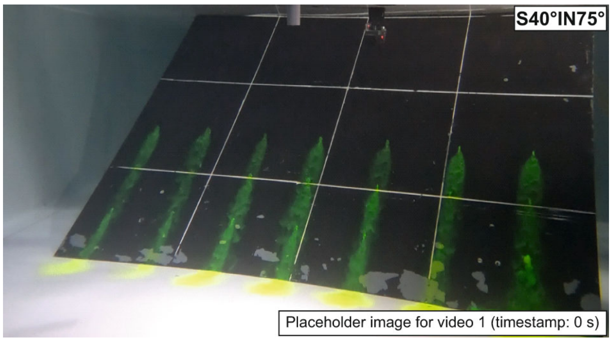

Video 1. Annotated video illustrating the behaviour of density currents upon incidence with an oblique topographic slope (Experiment S40°IN75°).

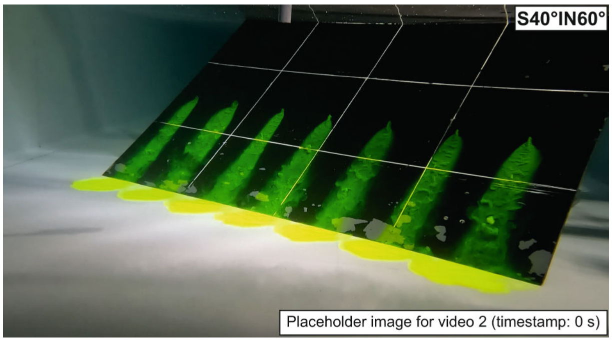

Video 2. Annotated video illustrating the behaviour of density currents upon incidence with an oblique topographic slope (S40°IN60°).

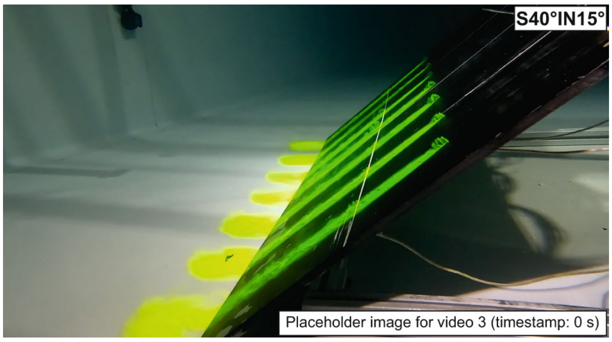

Video 3. Annotated video illustrating the behaviour of density currents upon incidence with an oblique topographic slope (Experiment S40°IN15°).

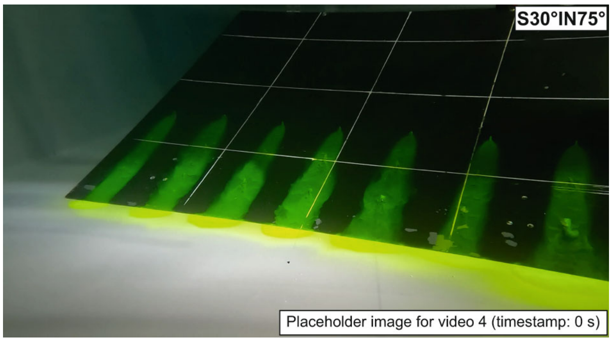

Video 4. Annotated video illustrating the behaviour of density currents upon incidence with an oblique topographic slope (Experiment S30°IN75°).

profiling using an ultrasonic velocity profiler (UVP); and (iii) density profiling using a siphon array. In the flow visualization run, overhead images were taken by a Fujifilm X-T4 camera with a Fujifilm 14 mm f/2.8R XF lens to capture the whole view of the experiment every second. Fluorescent purple dye was added to the input density current to aid flow visualization. To monitor the real-time flow properties (velocity and density) and provide a reference for the subsequent ramp experiments, velocity profiles collected by UVP and density profiles via a siphon system were obtained for flows at 3 m downstream from the channel mouth along the channel-basin centreline (i.e. the position of the base of the ramp in subsequent experiments; Fig. 1A).

UVP (Met-Flow, UVP DUO, 4 MHz; Met-Flow SA, Lausanne, Switzerland; Fig. 2A) was utilized to record the velocity field of the entire density current (cf. Takeda, 1991, 1993; Best *et al.*, 2001; Lusseyran *et al.*, 2003; Keevil *et al.*, 2006). A vertical array of 10 UVP probes was oriented parallel to the basin floor and positioned at 0.01, 0.02, 0.03, 0.04, 0.05, 0.06, 0.07, 0.09, 0.11 and 0.13 m, respectively, above the basin floor (Fig. 2A). Each UVP probe recorded the instantaneous downstream flow velocity at 128 measurement positions along its axis extending 10–29 cm from the probe head in the configuration used (see Table S1 for details of the UVP set up). Neutrally buoyant hollow glass spheres (Sphericel 110-P8; 10 μm diameter) were seeded into the inlet flow at a constant discharge rate via a peristaltic pump throughout the experimental run (cf. Thomas *et al.*, 2017; Ho *et al.*, 2019), in order to enhance reflection of the ultrasound signal. Additionally, the ambient water in front of the UVP probes was also seeded with the same glass spheres to increase the signal-to-noise ratio to *ca* 30 dB. This experiment started from the release of the inlet flow from the mixing tank and was shut off at *ca* 150 s.

13653091, 0, Downloaded from https://onlinelibrary.wiley.com/doi/10.1111/sed.70032 by Schweizerische Akademie Der, Wiley Online Library on [20/07/2025]. See the Terms and Conditions (https://onlinelibrary.wiley.com/terms-and-conditions) on Wiley Online Library for rules of use; OA articles are governed by the applicable Creative Commons License

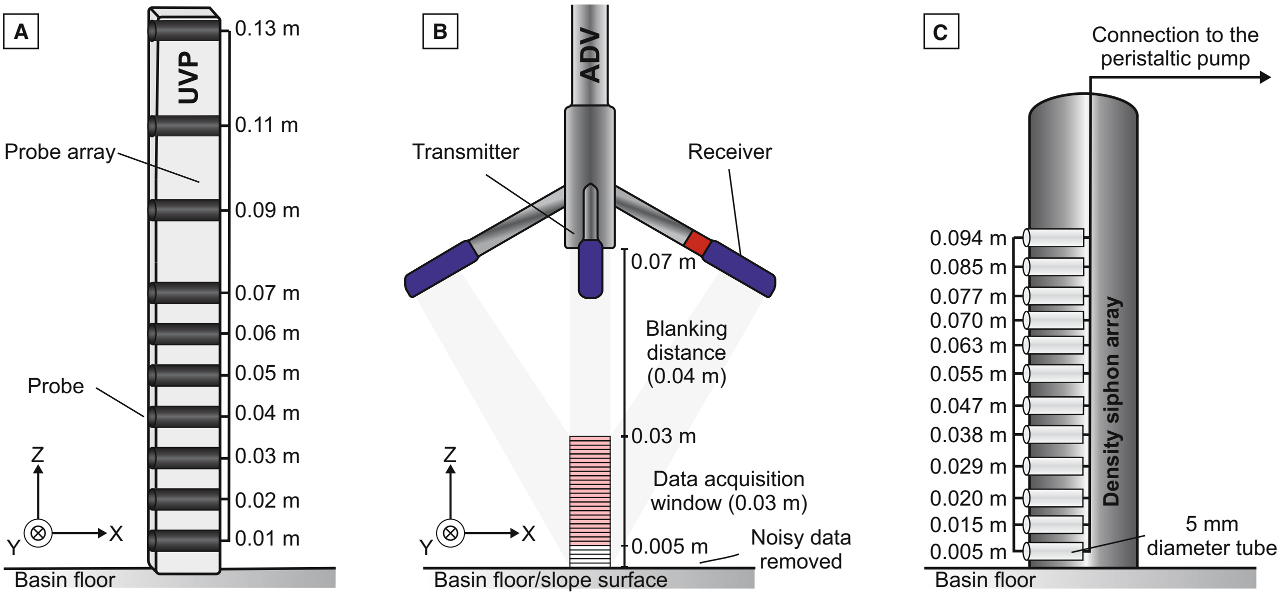

Fig. 2. Set up of (A) the UVP, (B) ADV and (C) siphoning systems in this study to measure the velocity and density profiles, respectively. All profiles were measured vertically to the basin floor, irrespective of whether the instrument was mounted above the basin floor or the slope surface. The siphon system was placed 3 m downstream of the channel mouth, on the centreline of the basin (see Fig. 1). See Fig. 1 and text for locations of the UVP and ADV positions.

Siphons were positioned along a vertical line and located at 0.005, 0.015, 0.020, 0.029, 0.038, 0.047, 0.055, 0.063, 0.070, 0.077, 0.085 and 0.094 m, respectively, above the basin floor (Fig. 2C). Fluid was extracted via a peristaltic pump at a constant flow rate (3.9 mL s^{-1} per siphon tube), with the rate chosen to balance obtaining enough fluid samples whilst minimizing perturbations to the *in situ* flow structure. After the experimental run, the density of the collected fluid samples was measured by the aforementioned portable densimeter.

Ramp experiments

In each ramp experimental configuration, three repeats were run using identical initial conditions but with different purposes, for example, flow visualization, and two sets of velocity profiling data using Acoustic Doppler velocimetry (ADV) systems. In these experiments, the inlet flow was shut off abruptly at *ca* 130 s after the start of the experiment.

In the flow visualization runs, each experiment was recorded using up to four high-resolution video cameras (GoPro, HERO 10; GoPro, Inc., USA). One was mounted at *ca* 2 m downstream from the channel mouth along the channel-basin centreline to capture the front view of the density current encountering the containing topography (i.e. ramp), two along the side of the ramp to capture the side view and one directly above the top of the ramp surface to capture the top view. No dye was added to the inlet flow as it would provide little information on the internal fluid motion within the current. Instead, Pliolite, a low-density and highly reflective polymer, and a small amount of white paint were added to the input current to help visualization (cf. Edwards *et al.*, 1994). The Pliolite has a subspherical shape, with a mean grain size of 1.5 mm and a density of 1050 kg m^{-3}. To improve the visualization of the density current interacting with the topographic ramp, fluorescent yellow dye streams (except for the parallel-flow-topography experiment shown in the Discussion, whereby fluorescent blue, yellow and purple dyes were injected from the rear of the ramp at different elevations, respectively; Video 5) with the same density as the inlet flow were injected via a series of tubes mounted from the rear of the ramp and flush with its surface. These tubes were located at three different elevations and distributed evenly on the ramp surface (i.e. 0.15 m, 0.30 m and 0.45 m away from the base of the ramp, respectively).

ADV (Nortek Vectrino Profiler; Nortek Inc., Rud, Norway; Fig. 2B) was used to capture the temporal evolution of the 3D velocity field of

© 2025 The Author(s). *Sedimentology* published by John Wiley & Sons Ltd on behalf of International Association of Sedimentologists,

13653091, 0, Downloaded from https://onlinelibrary.wiley.com/doi/10.1111/sed.70032 by Schweizerische Akademie Der, Wiley Online Library on [20/07/2025]. See the Terms and Conditions (https://onlinelibrary.wiley.com/terms-and-conditions) on Wiley Online Library for rules of use; OA articles are governed by the applicable Creative Commons License

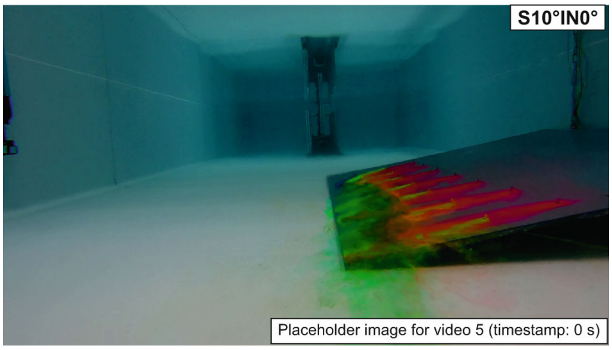

Video 5. Annotated video illustrating the behaviour of density currents upon incidence with a flow-parallel topographic slope of 10° slope gradient. Note that the flow has not reached the sidewalls of the tank prior to interacting with the slope. The interaction of the flow with the upstream edge of the topographic slope appears to generate a small effect at the proximal end of the slope; there is very little flow at the most upstream dye injection point. However, elsewhere the flow fluctuations are perpendicular to the slope, and so the proximal end of the slope is not affecting the flow dynamics significantly. The basic set up (e.g. the inlet flow conditions, the density of the main-tank water and initial water depth of the main tank) and run time of this experiment were the same as the other experiments in this study.

the flows at a near-bed region (i.e. a coverage of 0.03 m height above the basin floor or slope surface). ADV records three components of velocity in bins with a vertical resolution of 1 mm (see Table S1 for the details of the ADV set up). The ADV data constrain the 3D velocity structure of the flows through 100 Hz measurements of instantaneous velocities (cf. 4 Hz for the UVP; Table S1). The measurements of the near-bed velocity are critical to understanding the conditions that affect sediment transport and deposition. In each ramp experimental configuration, four ADVs were utilized to record the 3D flow velocity field at the near-bed region (Figs 1B–E and 2B). One was positioned above the basin floor, at 0.02 m upstream from the base of the ramp along the channel-basin centreline (ADV1) to capture the basal flow reversals. The other three (ADVs 2–4) were placed above the slope surface to capture the temporal evolution of the velocity field near the ‘flow front’ position (see *General flow behaviour* subsection). The exact locations of these three ADVs were carefully chosen based on the position of the ‘flow front’ observed from the flow visualization videos, which varied across different experiments. The transducers of the ADVs 1–4 were mounted vertically 0.07 m above either the basin floor (ADV1) or the slope surface (ADV2–4) and recorded the velocity profile in thirty-one 1-mm-high cells ranging from 0 to 0.03 m above the slope surface (Fig. 2B). Due to experimental constraints, two sets of ADV data (ADVs 1–2 and ADVs 3–4) were collected in separate runs with the same initial conditions, varying the measurement locations of the ADVs in each case. The four ADVs were subsequently integrated to visualize the 3D flow velocity field above and/or close to the base of the slope. During each measurement, synchronization of the two ADVs was achieved using Nortek’s MIDAS data acquisition software. The recording started from the release of the inlet flow and stopped at *ca* 240 s (this time duration is chosen to capture the waning phase of the flow). Neutrally buoyant hollow glass spheres were used for seeding in the same manner as the UVP runs.

Experimental data analysis

All the raw instantaneous velocity data collected by the UVP and ADV systems were post-processed in Matlab (cf. Buckee *et al.*, 2001; Keevil *et al.*, 2006; Keavney *et al.*, 2025). Firstly, data spikes in the time series that were more than two standard deviations from the mean were removed; here, the mean was estimated as an 11-point moving average. Secondly, the removed spike points were replaced by a 3-point moving mean. The ADV data closest to the basin floor or the slope surface were affected by excess noise because of reflections. Consequently, the plotted data were clipped so that the bottom five data points (<0.5 cm) were removed (Fig. 2B). This excess noise sometimes affected points as high as 0.7 cm above the bed, and thus for data analysis only the section between 0.7 and 3.0 cm above the basin floor or slope surface were utilized.

In this work, two sets of Cartesian coordinate systems were adopted, either relative to the basin floor or to the ramp (Fig. 1A and F). The filtered 3D velocity data after the first step were recalculated and expressed in one or the other of these two coordinate systems. When the former spatial coordinate system (Fig. 1A) is adopted, the 3D velocity components (u, v and w) are termed as streamwise (i.e. upstream and downstream), cross-stream and vertical velocities in the x, y and z directions, respectively. When the latter spatial coordinate system

13653091, 0, Downloaded from https://onlinelibrary.wiley.com/doi/10.1111/sed.70032 by Schweizerische Akademie Der, Wiley Online Library on [20/07/2025]. See the Terms and Conditions (https://onlinelibrary.wiley.com/terms-and-conditions) on Wiley Online Library for rules of use; OA articles are governed by the applicable Creative Commons License

is used (Fig. 1F), they are termed as longitudinal (i.e. up-slope and down-slope above the ramp, or outbound and return beyond the ramp), along-slope (i.e. strike) and vertical velocities in the x', y' and z' directions, respectively.

The filtered instantaneous velocity data collected by the ADV system are presented as velocity time series profiles. In these plots, positive values of longitudinal velocity depict flows travelling towards the ramp (outbound or up-slope flow), whereas negative ones depict flows travelling away from the ramp (return or down-slope flow). The maximum velocity ($U_{\max}$) is taken as the highest absolute value over the measured height range (0.7–3.0 cm) of the ADV profiles. The fluctuations in $U_{\max}$ are shown on the time series panels and serve as a representative longitudinal flow velocity magnitude.

Flow scaling and characterization

A generic Froude scaling modelling approach (Ashmore, 1991a, 1991b; Peakall *et al.*, 1996) is used in this work to ensure that the experimental saline density currents can be compared to natural systems. Froude-scale modelling (FSM) requires that the densimetric Froude number (Fr_d) in the experimental flows should be similar to natural systems, whilst the Reynolds number (Re) is relaxed, but still within the fully turbulent regime (Graf, 1971; Yalin, 1971; Peakall *et al.*, 1996). In a generic FSM approach, the experiments are based on a general comparison with the modelled geomorphic processes (Peakall *et al.*, 1996).

The Reynolds number, Re, is used to characterize whether the flow is laminar or turbulent and is expressed by the ratio between the inertial forces to the viscous forces. It is given by

$$Re = \frac{\rho_s U h}{\mu} \tag{1}$$

where ρ_s represents the depth-averaged density of the current, U is the depth-averaged velocity over the flow height, h is the flow height and μ is dynamic viscosity. Typically, flows with $Re > 2000$ are considered fully turbulent, flows with $Re < 500$ are laminar, and flows with $Re = 500$–2000 are transitional.

The densimetric Froude number in gravity currents accounts for the ratio between inertial forces and gravity/buoyancy forces (Kneller & Buckee, 2000), and is expressed as

$$Fr_d = \frac{U}{\sqrt{g' h}} \tag{2}$$

$$g' = \frac{g(\rho_s - \rho_a)}{\rho_a} \tag{3}$$

where g is gravitational acceleration, g' represents the reduced gravitational acceleration and ρ_a denotes the density of the ambient fluid. Typically, flows with $Fr_d > 1$ are considered supercritical whereas flows with $Fr_d < 1$ are subcritical, though the value of the critical densimetric Froude number (Fr_{dc}), denoted by $Fr_{dc} = 1$, may be different in stratified density currents (e.g. Huang *et al.*, 2009; Sumner *et al.*, 2013; Dorrell *et al.*, 2016).

Based on the no-ramp control experiment, the experimental density currents recorded at ~3 m downstream from the channel mouth along the channel-basin centreline (i.e. the position where the centrepoint of the base of the slope resides; Fig. 1A) were demonstrated to have a Reynolds number of 3203 and a densimetric Froude number of 0.50 (Table 2), and therefore were fully

Table 2. Summary of the flow characteristics for the experimental density current recorded at 3 m downstream from the channel mouth along the channel-basin centreline in the no-ramp reference experiment. Calculations of the mean depth-averaged downstream velocity and current density are detailed in Table S1.

Parameter	Value	Unit
Density of the ambient fluid (ρ_a)	999.58	kg m^{-3}
Dynamic viscosity (μ)	0.001	Pa s
Gravitational acceleration (g)	9.81	m s^{-2}
Reduced gravitational acceleration (g')	0.030	m s^{-2}
Flow depth (h)	0.11	m
Mean depth-averaged density of the current (ρ_s)	1002.6	kg m^{-3}
Mean depth-averaged downstream velocity (U)	0.029	m s^{-1}
Maximum downstream velocity (u_p)	0.059	m s^{-1}
Height of the maximum downstream velocity above the basin floor (h_p)	0.02	m
Reynolds number (Re)	3203	None
Densimetric Froude number (Fr_d)	0.50	None

13653091, 0, Downloaded from https://onlinelibrary.wiley.com/doi/10.1111/sed.70032 by Schweizerische Akademie Der, Wiley Online Library on [20/07/2025]. See the Terms and Conditions (https://onlinelibrary.wiley.com/terms-and-conditions) on Wiley Online Library for rules of use; OA articles are governed by the applicable Creative Commons License

turbulent and subcritical. Estimation of these two parameters is detailed in Data S1: SI1 (see also Keavney *et al*., 2025).

RESULTS

Gravity current evolution in the no-ramp experiment

Details on the evolution of the gravity current in the no-ramp experiment are presented in Keavney *et al*. (2025) and are summarized herein. The saline density current initially enters the confined channel section as a highly turbulent flow with a well-developed head region, which is followed by a stable, quasi-steady body region during the rest of the experimental run (Fig. 3A). On exiting the confined channel section, the flow starts to spread radially and symmetrically above the flat basin floor (Fig. 3B). Multiple lobes and clefts can be observed at the propagating head of the density current. A radial hydraulic jump can be observed immediately downstream of the channel-mouth location (Fig. 3D), suggesting that the flow regime has transitioned from a supercritical state in the channel section to a subcritical state in the horizontal basin floor (see also *Flow scaling and characterization* subsection). Finally, the abrupt termination of the inlet flow leads to a rapid decrease in current velocity and causes the current body to diminish quickly.

The representative time-averaged UVP downstream velocity profile obtained from the body region of the flows (averaging over 30 s; Fig. 3G) was recorded at 2.966 m downstream from the channel mouth along the channel-basin centreline (i.e. 0.034 m in front of the UVP probes). The instantaneous downstream velocity time series data for the flow recorded at the same position indicate a quasi-steady body of the flow with the arrival and waning of the flow at *ca* 30 s and 150 s, respectively. The time-averaged velocity profile of the flow (Fig. 3G) reveals a mean depth-averaged downstream velocity of 0.029 $\mathrm{m\,s^{-1}}$, a mean depth-averaged current density of 1002.6 $\mathrm{kg\,m^{-3}}$ (i.e. 0.3% excess density) and a flow height or thickness of *ca* 0.11 m (Table 2; Data S1: SI1). The downstream velocity reaches its maximum value ($u_p = 0.059\ \mathrm{m\,s^{-1}}$) at a height of 0.02 m above the basin floor ($h_p = 0.02$ m). The time-averaged flow density profile at 3 m downstream (Fig. 3G) exhibits a noticeable exponential decrease in excess density upward, with a highest flow density ($\rho_{si} = 1009\ \mathrm{kg\,m^{-3}}$; 0.9% excess density) near the basin floor ($h_i = 0.005$ m). The instantaneous density time series plot for the flow current at this position (Fig. 3H) reveals a distinct density interface separating a denser region near the basal part of the flow and a more dilute region in the upper part of the flow.

Interaction of gravity currents with containing topography in the ramp experiments

General flow behaviour

Here, experimental observations for Experiment S20°IN75° [slope angle (S) in degrees followed by incidence angle (IN) in degrees; Fig. 4] are described in detail to summarize the general flow behaviour when flows encounter the topographic slope. Once the flow exits the channel, it propagates along the basin as an unconfined underflow until encountering the containing slope (Fig. 4A). Upon incidence with the topographic slope, the flow decelerates and becomes strongly multidirectional on the slope surface (see *Temporal variability of flow direction at the near-bed region* subsection). Simultaneously, flow stratification promotes the original flow to be decoupled into two parts: a lower denser part and an upper less dense part. The dilute upper part of the flow runs up the slope surface and thins until reaching its maximum height H_{max} ('maximum run-up height', hereafter; cf. Pantin & Leeder, 1987; Edwards *et al*., 1994; Fig. 4C). This is termed as flow thinning and stripping on the slope surface hereafter. In contrast, the dense, lower region of the flow collapses back down the slope (Fig. 4C). The zone of flow stripping on the slope surface can be quantified by the height of the initial reversal of the dense lower flow H_{min} and the maximum run-up height H_{max}. Specifically, the lower limit of the flow stripping zone is quantified by the height upslope at which the basal region of the flow returns downslope because this marks the onset of flow thinning upslope. The initial reversal of the dense lower part of the flow can undercut the primary outbound flow and migrate upstream from the slope before eventually dissipating in the basin. No trains of upstream-migrating solitons or bores are visually observed in the experiments (cf. Pantin & Leeder, 1987; Edwards *et al*., 1994). Instead, the initial flow reversal of the basal part of the flow just above the containing slope leads to the development of

© 2025 The Author(s). *Sedimentology* published by John Wiley & Sons Ltd on behalf of International Association of Sedimentologists, *Sedimentology*

13653091, 0, Downloaded from https://onlinelibrary.wiley.com/doi/10.1111/sed.70032 by Schweizerische Akademie Der, Wiley Online Library on [20/07/2025]. See the Terms and Conditions (https://onlinelibrary.wiley.com/terms-and-conditions) on Wiley Online Library for rules of use; OA articles are governed by the applicable Creative Commons License

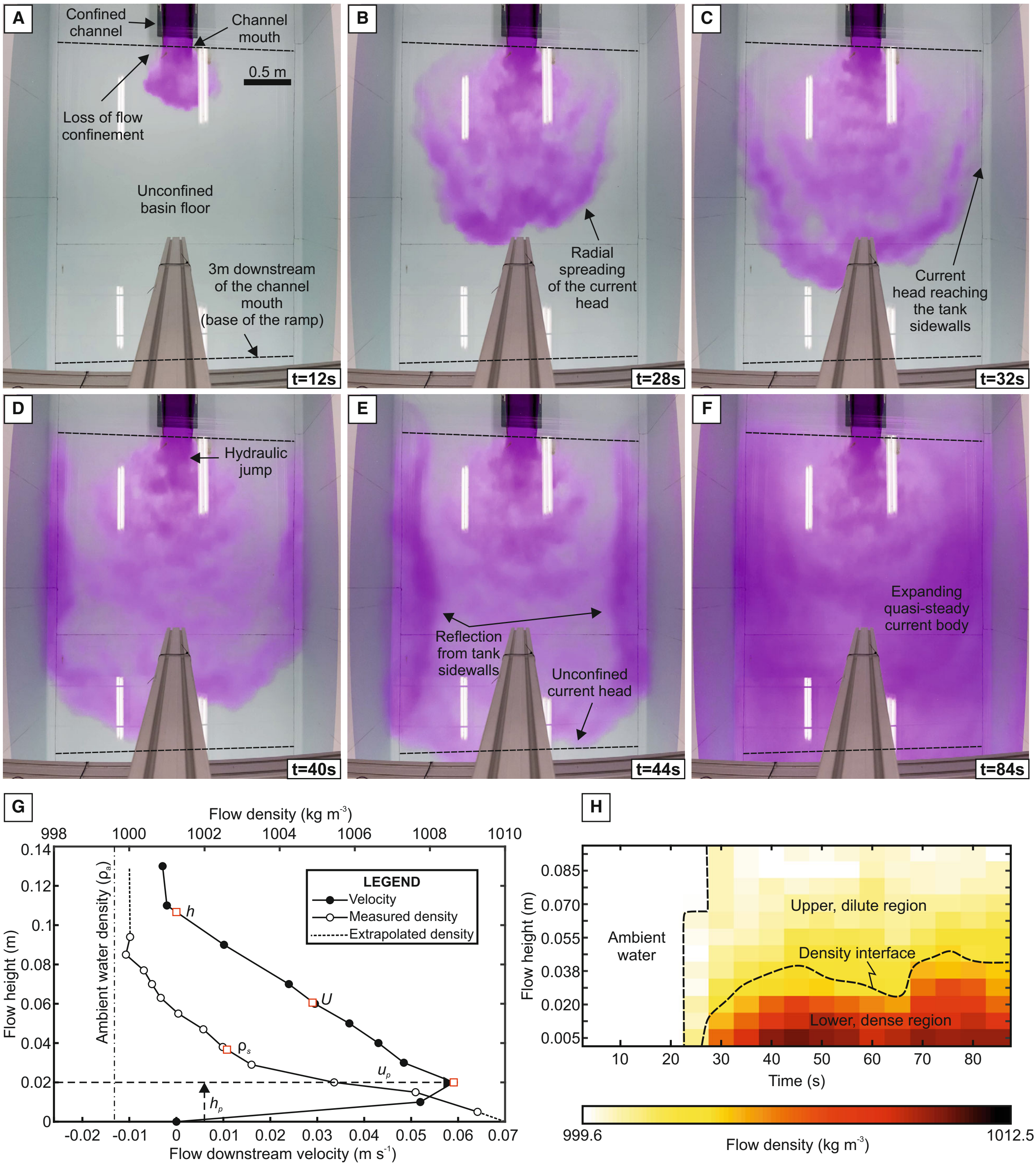

Fig. 3. (A–F) Set of overhead photographs illustrating the evolution of the saline density currents from the channel section to the basin floor in the no-ramp reference experiment. Note that a radial hydraulic jump was observed immediately downstream of the channel mouth. (G) Profiles of time-averaged flow downstream velocity (measured using the UVP) and density for the experimental density current recorded at 3 m downstream of the channel mouth along the channel-basin centreline in the no-ramp reference experiment. Both measurements were initiated 5 s after the current head passed and lasted for 30 s. The flow depth h, maximum downstream velocity u_p, its height above the basin floor h_p, depth-averaged downstream velocity U and depth-averaged density ρ_s are shown in the panel as red squares. The ambient water density was measured at 12°C. (H) Time series profiles of flow density measured at 3 m downstream of the channel mouth along the channel-basin centreline, the position of which is shown as a red circle in Fig. 1A.

© 2025 The Author(s). *Sedimentology* published by John Wiley & Sons Ltd on behalf of International Association of Sedimentologists, *Sedimentology*

13653091, 0, Downloaded from https://onlinelibrary.wiley.com/doi/10.1111/sed.70032 by Schweizerische Akademie Der, Wiley Online Library on [20/07/2025]. See the Terms and Conditions (https://onlinelibrary.wiley.com/terms-and-conditions) on Wiley Online Library for rules of use; OA articles are governed by the applicable Creative Commons License

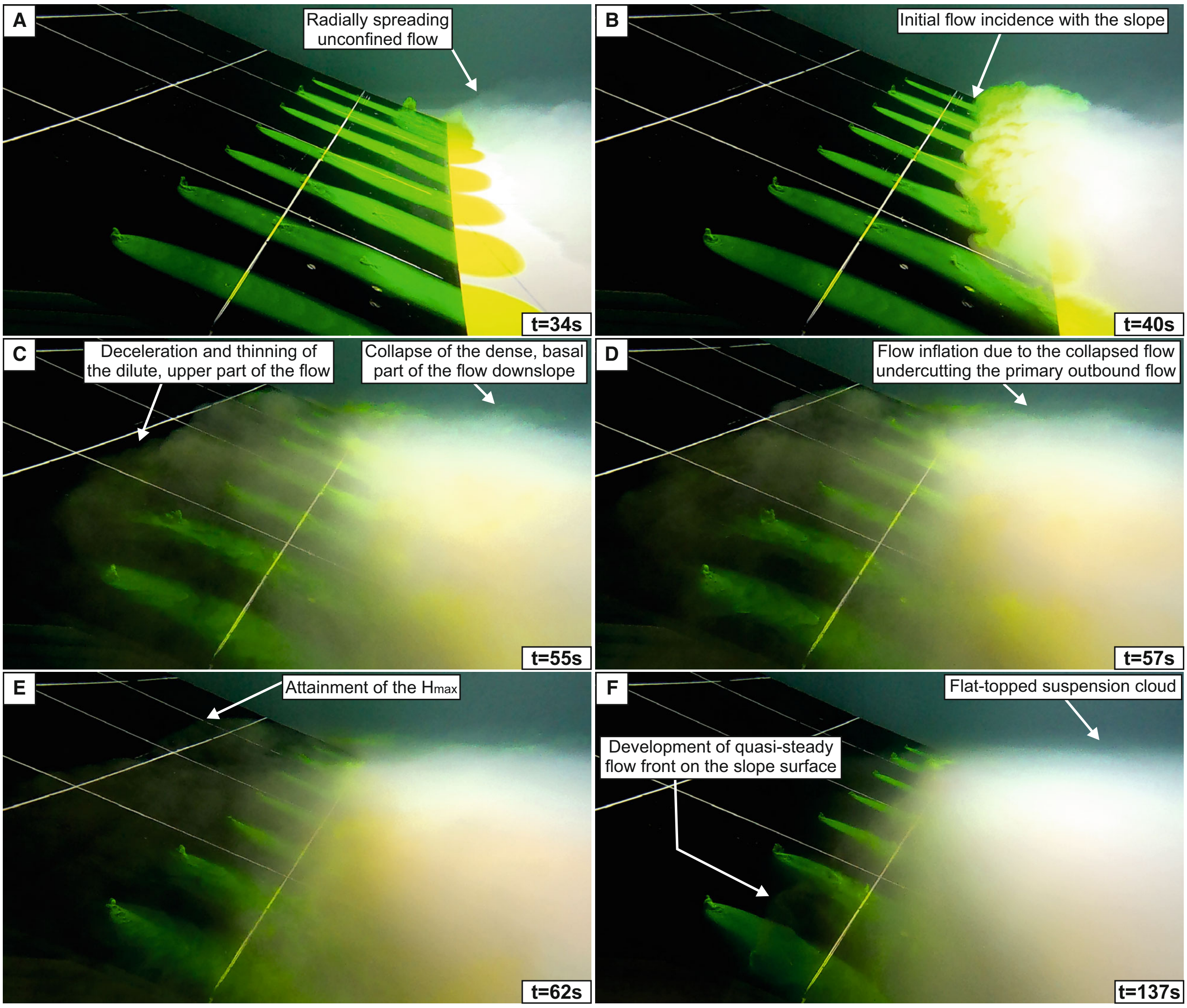

Fig. 4. Representative side-view photographs (A–F) depicting the temporal evolution of density currents upon incidence with an oblique topographic slope (e.g. Experiment S20°IN75°). $H_{\max}$ denotes the maximum height that the dilute, upper part of the flow can run up on the slope surface. *t* denotes the experimental time since the release of the flow from the mixing tank.

a bulge close to the ramp (referred to herein as flow inflation) (Fig. 4D). Subsequently, as the parental flow re-establishes, this initial flow inflation develops into a flat-topped suspension cloud (i.e. a sharp, sub-horizontal interface with the ambient water) present in the basin upstream of the ramp, and a quasi-stable 'flow front' develops on the slope surface (Fig. 4F). Note that for consistency, when flows run along a highly oblique or near parallel slope, the 'flow front' term is still used but annotated with quotation marks, which means the flow lateral margin, or flow top abutting against the slope. The suspension cloud migrates very slowly upstream [averaging *ca* 1 cm s^{-1} (maximum *ca* 2.8 cm s^{-1}) from initial flow reversal at *ca* 30–40 s]. Finally, the waning of the inlet flow causes the suspension cloud to collapse. Flow behaviour, including the degree of lateral flow expansion on the slope surface, the degree of flow thinning and stripping and the relative strength between flow deflection and reflection, varies as a function of both the slope gradient and the incidence angle of the flow onto the slope.

Variation of incidence angles of the current onto the slope. The effects of containing slope orientation, with respect to flow direction, on

13653091, 0, Downloaded from https://onlinelibrary.wiley.com/doi/10.1111/sed.70032 by Schweizerische Akademie Der, Wiley Online Library on [20/07/2025]. See the Terms and Conditions (https://onlinelibrary.wiley.com/terms-and-conditions) on Wiley Online Library for rules of use; OA articles are governed by the applicable Creative Commons License

flow behaviour were explored by systematically changing the incidence angles of the flow to the slope with the same slope gradient. Here, the results for three of the 18 experiments are presented: S40°IN75°, S40°IN60° and S40°IN15° (Videos 1–3).

In Experiment S40°IN75° (Video 1), upon encountering the topographic slope, the flow runs into the slope and results in a wide divergence in flow velocity directions on the slope surface. The area of lateral flow expansion on the slope surface is the largest among the three experiments. The maximum run-up height ($H_{\max} = 0.29$ m, *ca* 2.6 times the flow thickness) occurs in the middle of the ramp, whereas the height of initial flow reversal develops at *ca* 0.13 m, approximately 1.2 times the flow thickness. Due to the high degree of topographic containment generated by the oblique ramp orientation in this experiment, reflection of the dense, basal part of the current is the strongest among these three experiments. Part of the dense, basal part of the flow is deflected and runs parallel to the slope. This basal flow is diverted at the point of incidence to the slope into two directions towards the lateral edges of the slope, with the dividing streamline or plane (cf. Kneller & McCaffrey, 1999) at *ca* 0.56 m from the right edge of the ramp looking downstream.

In Experiment S40°IN60° (Video 2), relatively less flow is observed to be able to run up the slope and more of the flow is deflected towards the left and right lateral edges of the slope looking downstream, compared to Experiment S40°IN75°. The divergence in flow velocity directions on the slope surface is also less pronounced. The area of lateral flow expansion on the slope surface decreases markedly. $H_{\max}$ develops at the right edge of the ramp, at *ca* 0.24 m upslope, approximately 2.2 times the flow thickness; the height of initial flow reversal is 0.13 m upslope, approximately 1.2 times the flow thickness. Flow reflection at the basal part of the slope is less pronounced due to a decrease in the topographic containment (see also *Temporal velocity pulsing* subsection). Hence, basal flow deflection is stronger relative to flow reflection, in contrast to Experiment S40°IN75°. The dividing streamline of the deflected dense, basal region of the flow is *ca* 0.37 m from the right edge of the ramp.

In Experiment S40°IN15° (Video 3), the highly oblique ramp orientation results in the current mainly being deflected parallel to the base of the slope with extremely limited interaction between the current and slope surface (i.e. limited flow reflection or lateral flow expansion). The zone of flow thinning and stripping on the slope surface is negligible, with the height of initial flow reversal located at 0.12 m upslope, *ca* 1.1 times the flow thickness and maximum run-up height at 0.16 m upslope, *ca* 1.4 times the flow thickness.

Variation of slope gradient. The effects of slope gradient on flow behaviour were investigated using a single oblique incidence angle. Here, the results for three of the 18 ramp experiments are presented: S20°IN75°, S30°IN75° and S40°IN75° (Fig. 4 for Experiment S20°IN75°, Videos 1 and 4 for Experiment S40°IN75° and S30°IN75°, respectively).

Results in Experiment S40°IN75° were described in the preceding section. In Experiment S30°IN75° (Video 4), upon encountering the containing slope, the flow strikes the slope less strongly and becomes multidirectional on the slope surface but with a much larger area of lateral flow expansion, compared to Experiment S40°IN75°. $H_{\max}$ occurs laterally at *ca* 0.37 m away from the right edge of the ramp, and *ca* 0.36 m upslope, approximately 3.3 times the flow thickness; the height of initial flow reversal is *ca* 0.12 m upslope, approximately 1.1 times the flow thickness. The strength of the flow reflection is not apparent in the visualization video. However, the deflection of the dense, basal part of the flow can be identified. The basal flow is deflected into two directions towards the two lateral edges of the slope, respectively, with the dividing streamline *ca* 0.56 m from the right edge of the ramp.

In Experiment S20°IN75° (Fig. 4), a much larger area of lateral flow expansion on the slope surface is observed, compared to the equivalent 30° and 40° slope experiments. $H_{\max}$ occurs laterally at *ca* 0.37 m away from the right edge of the ramp, and *ca* 0.26 m upslope, approximately 2.4 times the flow thickness; the height of initial flow reversal is *ca* 0.1 m upslope, approximately equal to the flow thickness. Like the case in Experiment S30°IN75°, the strength of flow reflection cannot be identified visually, but part of the basal flow is deflected to run parallel to the slope.

Temporal velocity pulsing

From the flow visualization videos, a series of upstream-migrating velocity reversals in the basal part of the flow can be identified, above

13653091, 0, Downloaded from https://onlinelibrary.wiley.com/doi/10.1111/sed.70032 by Schweizerische Akademie Der, Wiley Online Library on [20/07/2025]. See the Terms and Conditions (https://onlinelibrary.wiley.com/terms-and-conditions) on Wiley Online Library for rules of use; OA articles are governed by the applicable Creative Commons License

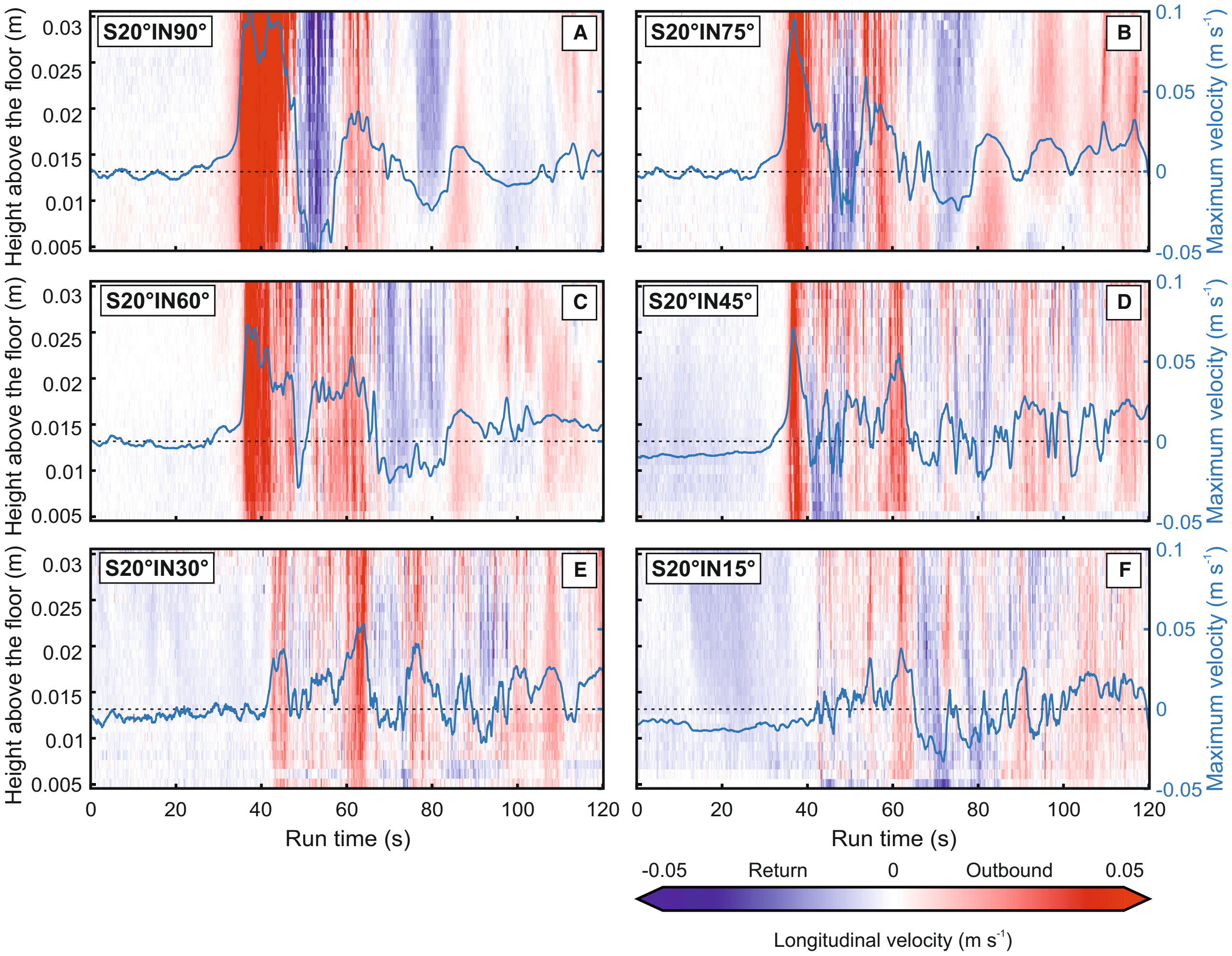

Fig. 5. Longitudinal velocity time series of the density currents recorded at the base of the slope along the channel-basin centreline (ADV1 in Fig. 1) for the ramp experiments [i.e. S20°IN90° (A), S20°IN75° (B), S20°IN60° (C), S20°IN45° (D), S20°IN30° (E) and S20°IN15° (F)]. For visualization, the data are clipped at $z \sim 0.5$ cm due to excess noise caused by reflections. Positive values of the longitudinal velocity depict flows travelling towards the ramp, whereas negative values depict flows travelling away from the ramp and back towards the inlet. The temporal evolution of maximum velocity up/down the ramp, U_{max}, [i.e. the highest value over the measured height range (0.7–3.0 cm) of the ADV profiles] is also shown (blue solid lines).

the flat basin floor near the base of the slope, and on the slope surface (Videos 1–4). Furthermore, the depth-constrained ADV longitudinal velocity time series profiles (Figs 5–8) capture the velocity reversals quantitatively at a point.

Base of slope: Reflection and basal flow reversal. Longitudinal velocity time series profiles of the flow recorded near the base of slope along the channel-basin centreline (Figs 5 and 6) exhibit multiple basal flow reversals when the flow encounters the topographic slope. Notably, the first basal flow reversal is of high velocity and highly turbulent, which is succeeded by a series of weaker basal flow reversals. After the first basal flow reversal diminishes, the second reversal typically re-establishes from an initially very low velocity to a final high velocity. The velocity of each reversal is generally lower than the preceding one. Nevertheless, the magnitude of the velocity, the number of velocity pulses and the duration of each pulse are different across the ramp experiments, as a function of both incidence angle and slope gradient.

Base of slope: Variation of incidence angles of the current onto the slope—Variation of incidence angle as a function of a single slope

© 2025 The Author(s). *Sedimentology* published by John Wiley & Sons Ltd on behalf of International Association of Sedimentologists, *Sedimentology*

13653091, 0, Downloaded from https://onlinelibrary.wiley.com/doi/10.1111/sed.70032 by Schweizerische Akademie Der, Wiley Online Library on [20/07/2025]. See the Terms and Conditions (https://onlinelibrary.wiley.com/terms-and-conditions) on Wiley Online Library for rules of use; OA articles are governed by the applicable Creative Commons License

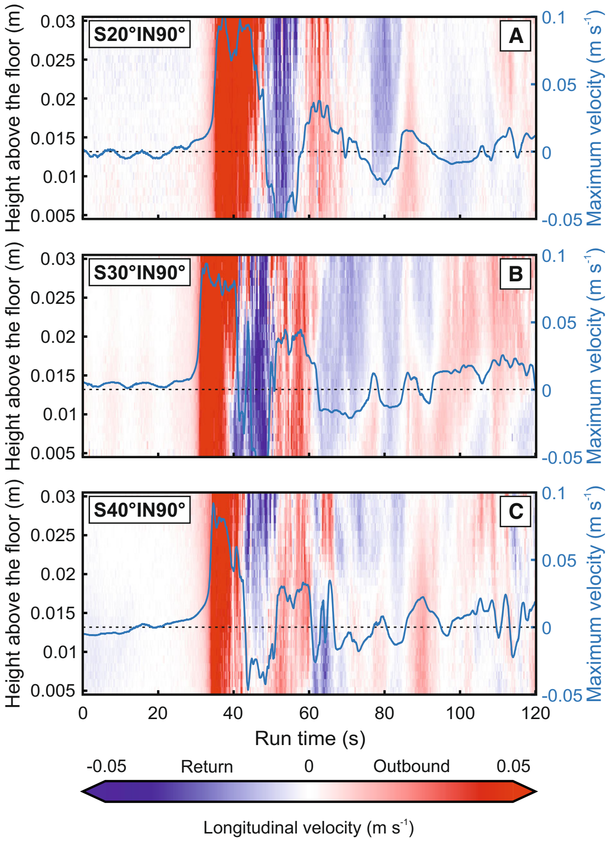

Fig. 6. Longitudinal velocity time series of the density currents recorded at the base of the slope along the channel-basin centreline (ADV1 in Fig. 1) for the ramp experiments [i.e. S20°IN90° (A), S30°IN90° (B) and S40°IN90° (C)]. For visualization, the data are clipped at $z \sim 0.5$ cm due to excess noise caused by reflections. Positive values of the longitudinal velocity depict flows travelling towards the ramp, whereas negative values depict flows travelling away from the ramp and back towards the inlet. The temporal evolution of maximum velocity up/down the ramp, $U_{\max}$, [i.e. the highest value over the measured height range (0.7–3.0 cm) of the ADV profiles] is also shown (blue solid lines).

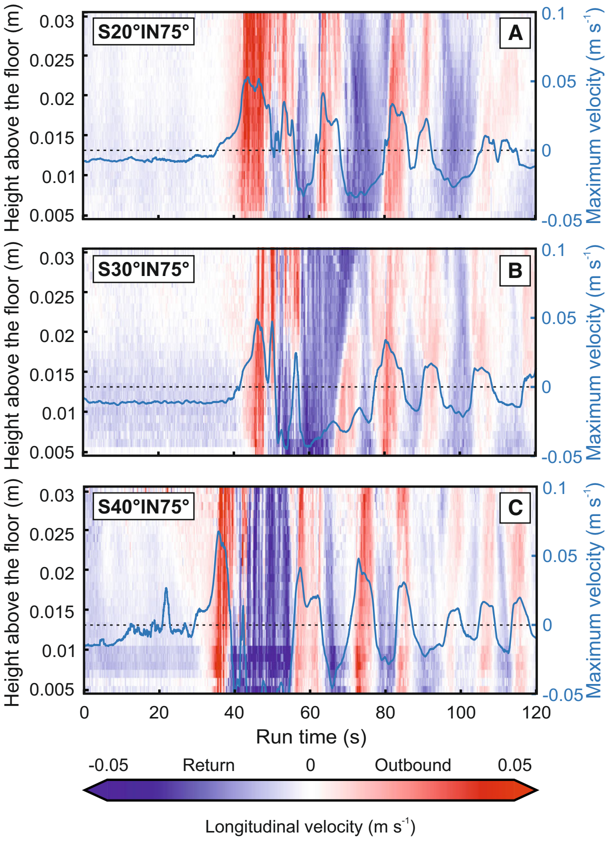

Fig. 7. Longitudinal velocity time-series of the density currents recorded at the 'flow front' position just above the slope surface (ADV3 in Fig. 1) for the ramp experiments [i.e. S20°IN75° (A), S30°IN75° (B) and S40°IN75° (C)]. For visualization, the data are clipped at $z \sim 0.5$ cm due to excess noise, caused by reflections. The temporal evolution of maximum velocity up/down the ramp, $U_{\max}$, [i.e. the highest value over the measured height range (0.7–3.0 cm) of the ADV profiles] is also shown (blue solid lines).

gradient (20°) is examined for experiments S20°IN90°, S20°IN75°, S20°IN60°, S20°IN45°, S20°IN30° and S20°IN15° (Fig. 5). Notably, for lower incidence angles, the magnitude of the maximum longitudinal velocity $U_{\max}$ markedly decreases ($U_{\max} = 0.06$–0.008 m s^{-1} for the basal flow reversals in Experiment S20°IN90° and $U_{\max} =$ 0.03–0.01 m s^{-1} in Experiment S20°IN15°). Furthermore, the velocity pattern tends to be characterized by more pulses ($N = 3$ for the basal flow reversals in Experiment S20°IN90° and $N > 7$ in Experiment S20°IN15°) and shorter time duration of each pulse ($T = 8$–12 s for the basal flow reversals in Experiment S20°IN90° and $T = 2$–7 s in Experiment S20°IN15°).

Base of slope: Variation of slope gradients—For cases across different slope gradients, results of the experiments S20°IN90°, S30°IN90° and S40°IN90° are presented (Fig. 6). In Experiment S20°IN90° (Fig. 6A), the first basal flow reversal begins *ca* 13 s after the arrival of the first outbound flow and subsequently sustains for *ca* 10 s until the re-establishment of the second outbound flow. The maximum magnitude of the first velocity reversal reaches *ca* 0.06 m s^{-1}. This is followed by four weaker flow reversals, with

13653091, 0, Downloaded from https://onlinelibrary.wiley.com/doi/10.1111/sed.70032 by Schweizerische Akademie Der, Wiley Online Library on [20/07/2025]. See the Terms and Conditions (https://onlinelibrary.wiley.com/terms-and-conditions) on Wiley Online Library for rules of use; OA articles are governed by the applicable Creative Commons License

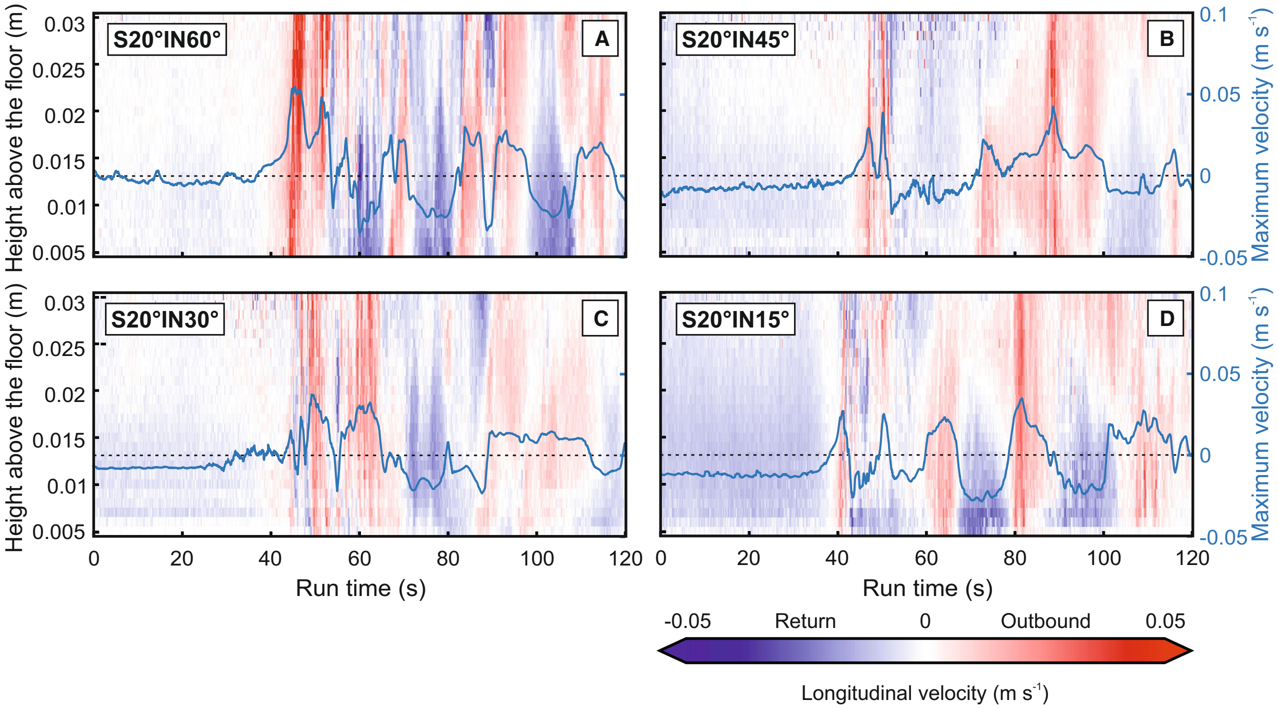

Fig. 8. Longitudinal velocity time series of the density currents recorded at the 'flow front' position just above the slope surface (ADV3 in Fig. 1) for the ramp experiments [i.e. S20°IN60° (A), S20°IN45° (B), S20°IN30° (C) and S20°IN15° (D)]. For visualization, the data are clipped at $z \sim 0.5$ cm due to excess noise, caused by reflections. The temporal evolution of maximum velocity up/down the ramp, $U_{\max}$, [i.e. the highest value over the measured height range (0.7–3.0 cm) of the ADV profiles] is also shown (blue solid lines).

time duration of each pulse of 11, 12, 3 and 1.4 s respectively and $U_{\max}$ ranging from 0.005 to 0.026 m s^{-1}. In Experiment S30°IN90° (Fig. 6B), the first basal flow reversal arrives at 9 s after the first outbound flow initially establishes, which then sustains for *ca* 8 s with a recorded downdip maximum velocity of 0.06 m s^{-1}. This is succeeded by three weaker flow reversals, with time duration of each pulse of 14, 6 and 4 s respectively and $U_{\max}$ ranging from 0.011 to 0.023 m s^{-1}. In Experiment S40°IN90° (Fig. 6C), the first basal flow reversal starts to develop at 10 s after the arrival of the first outbound flow, which then sustains for *ca* 5.5 s with a recorded downdip maximum velocity of 0.04 m s^{-1}. This is succeeded by seven weaker flow reversals, with time duration of each pulse of 4, 4.4, 6, 5, 3, 2 and 3 s respectively and $U_{\max}$ ranging from 0.008 to 0.026 m s^{-1}. For cases across different slope gradients, the magnitude of the maximum velocity shows minimal difference. However, experiments with a higher angle of slope gradient are demonstrated to be dominated by more velocity pulses and shorter time duration of each pulse. This suggests that the higher downslope gravitational component on steeper slopes leads to more frequent flow reflection.

In summary, the incidence angle of the current relative to the containing slope exerts a much stronger control on the velocity pulsing pattern of the flow near the base of the slope (e.g. the strength and time duration of each basal flow reversal) than the slope gradient.

On the slope: 'Flow front' velocity fluctuation. During the quasi-steady phase of each ramp experiment, a quasi-stable 'flow front' develops on the slope surface, which fluctuates over a short distance up-slope (Fig. 4F). Fluctuations of the 'flow front' velocity are examined quantitatively via the depth-constrained ADV longitudinal velocity time series profiles positioned at the centreline of the ramp (ADV3 in Fig. 1; Figs 7 and 8). Compared to measurements located at the base of the slope, the velocity magnitude of the 'flow front' is lower. The velocity structure, number of velocity pulses and time duration of each pulse

© 2025 The Author(s). *Sedimentology* published by John Wiley & Sons Ltd on behalf of International Association of Sedimentologists, *Sedimentology*

13653091, 0, Downloaded from https://onlinelibrary.wiley.com/doi/10.1111/sed.70032 by Schweizerische Akademie Der, Wiley Online Library on [20/07/2025]. See the Terms and Conditions (https://onlinelibrary.wiley.com/terms-and-conditions) on Wiley Online Library for rules of use; OA articles are governed by the applicable Creative Commons License

(Figs 7 and 8) are a function of both the incidence angle of the flow and the slope gradient.

For cases with different slope gradients (S20°IN75°, S30°IN75° and S40°IN75°), the magnitude of the maximum longitudinal velocity $U_{\max}$ exhibits only small variation, between -0.05 and $0.07\,\mathrm{m\,s^{-1}}$ (Fig. 7). Experiments with a steeper slope gradient configuration are associated with relatively more velocity pulses and shorter time duration of each pulse, albeit the differences are small.

Considering experiments S20°IN75°, S20°IN60°, S20°IN45°, S20°IN30° and S20°IN15°, those with a lower flow incidence angle tend to show comparatively fewer and longer duration velocity pulses (Figs 7 and 8). The velocity pulse patterns are irregular, that is, non-periodic. $U_{\max}$ does not vary markedly between cases with different incidence angle configurations. For example, -0.035–$0.05\,\mathrm{m\,s^{-1}}$ in Experiment S20°IN75° and $-$ 0.04–0.03 $\mathrm{m\,s^{-1}}$ in Experiment S20°IN15°.

Streamline analysis and power spectral analysis. In order to examine the nature of the temporal velocity pulsing in more detail, plots of streamlines in time of instantaneous longitudinal and vertical velocity are presented for the body of the flow, based on the ADV measurements. The channel-basin centreline at the base of slope, and the central 'flow front' position on the slope surface, in Experiment S20°IN75° and Experiment S20°IN90°, respectively, are utilized (Figs 9 and S1). The quasi-steady region of the current is chosen, from the passing of the current head to the current slowing down (a time window of 60 s). A major uncertainty is that the marked three-dimensional variation in flow fields observed in the experiments means there will be motion in or out of the plane (see *Temporal variability of flow direction at the near-bed region* section). In both orthogonal and oblique experimental settings, there are periods with multiple flow structures per flow reversal, over the height interval covered by the ADV in this physical experiment, whilst in other periods, variations in vertical streamlines are on approximately the same scale as the flow reversals. The structures are frequently variable and irregular and are unlike those interpreted as internal gravity waves in well-controlled two-dimensional flume tank experiments (e.g. Marshall *et al.*, 2021, their fig. 5).

To further assess whether the structures identified in the streamline analysis might be internal waves, single-sided amplitude spectral analysis using a Fast Fourier Transform (FFT) of the ADV time series longitudinal velocity is undertaken (cf. Dorrell *et al.*, 2018; Experiment S20°IN75° as an example; Fig. 10). Internal gravity waves are most likely to propagate on: (i) the steepest density gradient contrast (e.g. Patacci *et al.*, 2015; Lloyd *et al.*, 2022), (ii) the flow-ambient interface (e.g. Kneller *et al.*, 1991), or (iii) at the position of $U_{\max}$ (Marshall *et al.*, 2021, 2023). Given the ADV data do not cover the flow-ambient interface, and detailed density data on the slope are not available, the FFT analysis utilizes the position of $U_{\max}$. The position of $U_{\max}$ is variable and not always captured within the ADV dataset, but positioned towards the upper part of the measured flow (e.g. in Fig. 9). At the base of the slope, the $U_{\max}$ position approximates to the steepest density interface at the central position at the base of the ramp (albeit where density measurements were collected in the no-ramp run; Fig. 3H). Very low frequency oscillations in the range of *ca* 10^{-1} to 10^{0} Hz are observed for longitudinal velocity measurements at the central base of the ramp (Fig. 10H). The power spectra increase markedly with height upslope at the 'flow front' positions, with relatively higher but still low velocity frequency oscillations in the range of *ca* 10^{-1} to 10^{0} Hz at the left and central 'flow front' positions (Fig. 10E and 10F). Overall, there is a lack of distinct peaks in the frequency spectra that might coincide with internal waves, reinforcing the lack of internal waves seen visually.

Temporal variability of flow direction at the near-bed region

Temporal variability of the flow velocity vector (based on downstream and cross-stream velocity, that is, projected in the horizontal basin-floor plane) of the current recorded at 0.01 m above the basin floor and/or the slope surface is examined for each ramp experiment (Figs 11–14). A specific height of 0.01 m was chosen to avoid any possible noise-induced interference, whilst focusing on the near-bed velocity as this is critical for sediment transport and deposition processes.

Flow directions at the quasi-steady phase (34–120 s). Measurements during the quasi-steady phase of the current (Figs 11–13) indicate that all ramp experimental configurations record complex patterns of flow direction and magnitude, including the presence of multidirectional combined flow regimes above the slope surface

13653091, 0, Downloaded from https://onlinelibrary.wiley.com/doi/10.1111/sed.70032 by Schweizerische Akademie Der, Wiley Online Library on [20/07/2025]. See the Terms and Conditions (https://onlinelibrary.wiley.com/terms-and-conditions) on Wiley Online Library for rules of use; OA articles are governed by the applicable Creative Commons License

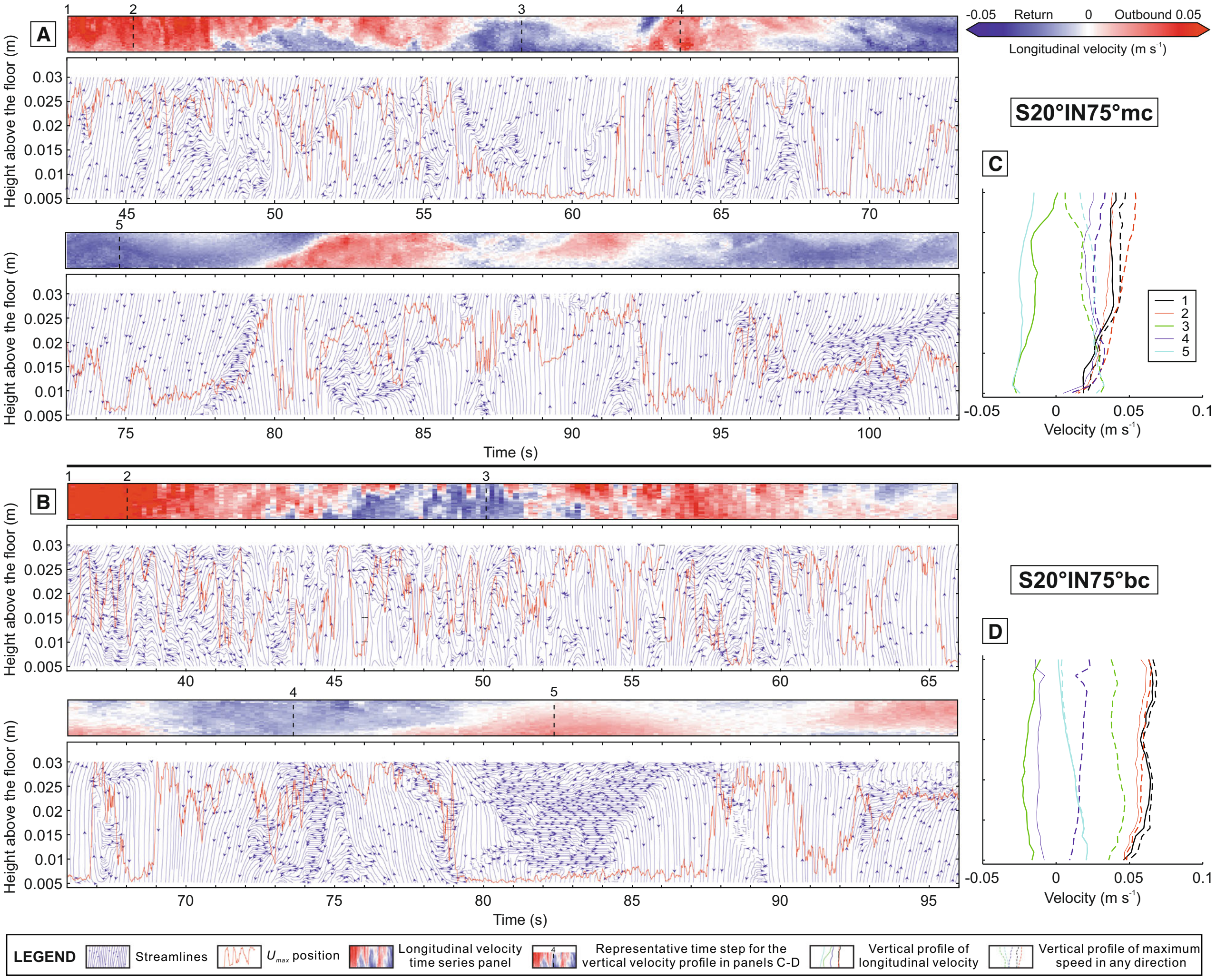

Fig. 9. (A, B) Plots of velocity streamlines as a function of time for Experiment S20°IN75°. The plots utilize Acoustic Doppler velocity profiler (ADV) instantaneous longitudinal and vertical velocity measurements. The temporal evolution of the position of the maximum longitudinal velocity, $U_{\max}$, [i.e. the highest absolute value over the measured height range (0.5–3.0 cm) of the ADV profiles] is also shown (red solid lines). This line is smoothed by applying a moving average over a window of 10 points. Note that in the case where $U_{\max}$ resides at the highest elevation of the ADV measurements (0.03 m), this may mean that the $U_{\max}$ of the full current is not captured by the ADV profile. Arrows on the streamlines directed to the right and left indicate flow travelling outbound and returning towards the inlet, respectively. 'bc' denotes the ADV measurements at the base of slope along the channel-basin centreline and 'mc' denotes the ADV measurements at the central 'flow front' position on the slope surface (in the flow direction), respectively (ADV3 in Fig. 1). For reference, the corresponding longitudinal velocity time series is also shown as a coloured band above the streamline panels (left); the scale is shown at top right. (C, D) Vertical profiles of the longitudinal velocity (solid lines) and the maximum measured velocity in any direction (dashed lines) at several representative time steps throughout the experimental run (right); these correspond to the numbered intervals on the left time series panels.

and near the base of slope (also see *Spatial variation of combined flows on slopes* subsection for details).

For the ramp experiments (Fig. 11), flow velocity is higher at the base of slope than that at the 'flow front' positions above the slope surface (e.g. maximum velocity of *ca* 0.09 m s^{-1} versus *ca* 0.05 m s^{-1} in Experiment S20°IN75°). Current directions recorded at the 'flow front' positions all exhibit a broadly radial dispersal pattern over the duration of the quasi-steady phase of the flow whilst those recorded at the base of slope along the channel-basin centreline typically demonstrate weaker radial distribution

© 2025 The Author(s). *Sedimentology* published by John Wiley & Sons Ltd on behalf of International Association of Sedimentologists, *Sedimentology*

13653091, 0, Downloaded from https://onlinelibrary.wiley.com/doi/10.1111/sed.70032 by Schweizerische Akademie Der, Wiley Online Library on [20/07/2025]. See the Terms and Conditions (https://onlinelibrary.wiley.com/terms-and-conditions) on Wiley Online Library for rules of use; OA articles are governed by the applicable Creative Commons License

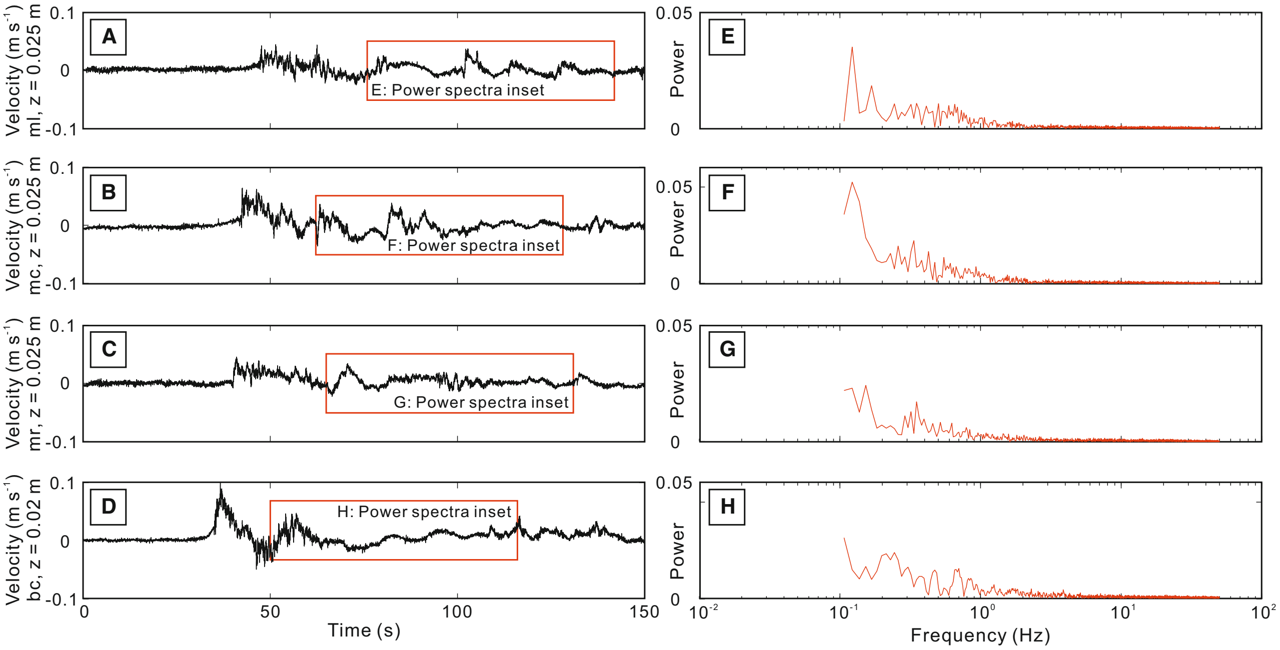

Fig. 10. Acoustic Doppler velocity profiler (ADV) longitudinal velocity time series (A–D) and associated single-sided amplitude spectrum of the longitudinal velocity fluctuations (E–H) for Experiment S20°IN75°. 'bc' denotes the measurements at the base of slope along the channel-basin centreline and 'ml', 'mc' and 'mr' denote the measurements at the left, central and right 'flow front' positions on the slope surface (in the flow direction), respectively (ADV4, ADV3 and ADV2 in Fig. 1). z denotes the height above the basin floor/slope surface. For the measurements at the 'flow front' positions, $z = 0.025$ m is chosen as this is indicated to be the position of $U_{\max}$ (Fig. 9) and can be associated with the development of putative internal waves in physical experiments (Marshall *et al.*, 2021, 2023). The position of $U_{\max}$ whilst variable, and not always captured within the ADV dataset, is towards the upper part of the measured flow (Fig. 9). Similarly, at the base of slope, the $U_{\max}$ position, which is again highly variable (Fig. 9), is taken here to be 0.02 m for the power spectra analysis, equivalent to the steepest density interface and $U_{\max}$ position recorded at the central position at the base of the ramp (albeit where instantaneous density measurements and downstream velocities were collected in the unconfined run; Fig. 3G, H). The red inset boxes in panels A–D indicate the time interval whereby the single-sided amplitude spectrum of the longitudinal velocity fluctuations is estimated.

and more unidirectional distribution patterns (Figs 11–13, see the descriptions below).

Across experiments with different flow incidence angles onto the slope (Fig. 12), the base of slope flow directions show a gradual transition from a radial to a more unidirectional dispersal pattern (oriented to the along-slope direction parallel to the slope) as the flow incidence angle decreases (Fig. 12E–H; 0°–360° in Experiment S20°IN90° with mean flow angles nearly orthogonal to the topographic slope strike or orientation; 320°–30° clockwise in Experiment S20°IN15° with flow angles in the range of *ca* 30° relative to the slope strike or orientation and mean flow angles nearly parallel to the slope strike). On the slope, the unidirectional component of the flow recorded at the central 'flow front' position increases with a lower incidence angle, although all configurations exhibit a radial dispersal pattern (Fig. 12A–D). Reflected flow orthogonal to the slope is seen at times on the slope, at the highest incidence angles (90° and 75°), but is a very infrequently present and of very low velocity at lower incidence angles (45° and 15°). At the base of slope, orthogonal reflected flow is not seen for the lower incidence angles (45° and 15°), barely observed for 75°, and thus dominantly restricted to the 90° incidence angle.

Across experiments with different slope gradients (Fig. 13), the velocity magnitude and the flow direction distribution do not vary markedly. Notably, with a steeper slope gradient, the velocity magnitude recorded at the base of slope or near the 'flow front' tends to be slightly larger. Furthermore, for steeper slopes, typically the current data exhibit a slightly wider spread in both overall flow directions throughout the

© 2025 The Author(s). *Sedimentology* published by John Wiley & Sons Ltd on behalf of
International Association of Sedimentologists, *Sedimentology*

13653091, 0, Downloaded from https://onlinelibrary.wiley.com/doi/10.1111/sed.70032 by Schweizerische Akademie Der, Wiley Online Library on [20/07/2025]. See the Terms and Conditions (https://onlinelibrary.wiley.com/terms-and-conditions) on Wiley Online Library for rules of use; OA articles are governed by the applicable Creative Commons License

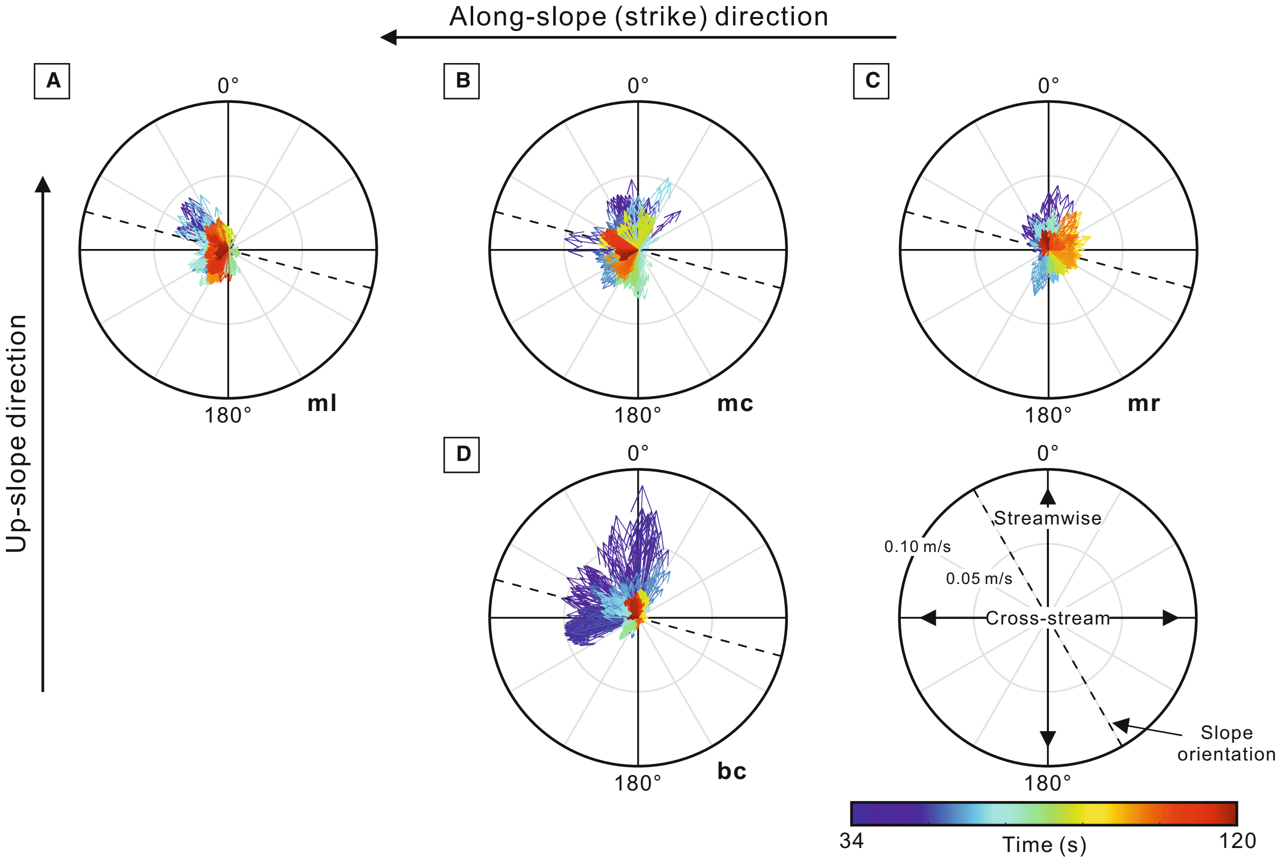

Fig. 11. Compass plots illustrating the spatial and temporal variability of the flow velocity vector (projected in the horizontal basin-floor) of the current within the quasi-steady phase (34–120 s) recorded at 0.01 m above the basin floor (D) and/or the slope surface (A–C) in Experiment S20°IN75°. 'bc' denotes the measurements at the base of slope along the channel-basin centreline and 'ml', 'mc' and 'mr' denote the measurements at the left, central and right 'flow front' positions (in the flow direction), respectively (ADV4, ADV3 and ADV2 in Fig. 1). In each compass plot, the arrow length denotes the velocity magnitude, and the direction denotes the velocity direction relative to the basin. Each arrow is colour coded as time. Black dashed line indicates the slope orientation. For presentation purposes, in each compass plot, the original 100 Hz ADV velocity data are decimated to 10 Hz.

experiment (290°–15° clockwise in Experiment S20°IN45° with flow angles in the range of *ca* 20–45° relative to the slope strike or orientation versus 290°–30° clockwise in Experiment S40°IN45° with flow angles in the range of *ca* 20–75° relative to the slope strike or orientation) and flow directions over a given period, compared to gentler topographic slopes. At a 45° incidence angle there is very little in the way of orthogonal reflected flow in any position, irrespective of slope angle.

In summary, the incidence angle of the current relative to the containing slope influences the temporal variability of the flow direction at the near-bed region more strongly than the slope gradient. This holds true both for the flow at the base of slope and the 'flow front' position along the channel-basin centreline.

Flow directions at the waning phase (160–-180 s). Temporal variability of the near-bed velocity vector above the slope surface during the waning phase of the current (Fig. 14) is analysed. This stage is critical for the sediment deposition process, especially the development of tractional bedforms such as ripples in the Bouma C division, which in field studies are compared to sole structure orientation to interpret the presence and orientation of seafloor topography (e.g. Kneller *et al.*, 1991; Hodgson & Haughton, 2004). This specific time window (160–180 s) exhibits velocities that are about

© 2025 The Author(s). *Sedimentology* published by John Wiley & Sons Ltd on behalf of International Association of Sedimentologists, *Sedimentology*

13653091, 0, Downloaded from https://onlinelibrary.wiley.com/doi/10.1111/sed.70032 by Schweizerische Akademie Der, Wiley Online Library on [20/07/2025]. See the Terms and Conditions (https://onlinelibrary.wiley.com/terms-and-conditions) on Wiley Online Library for rules of use; OA articles are governed by the applicable Creative Commons License

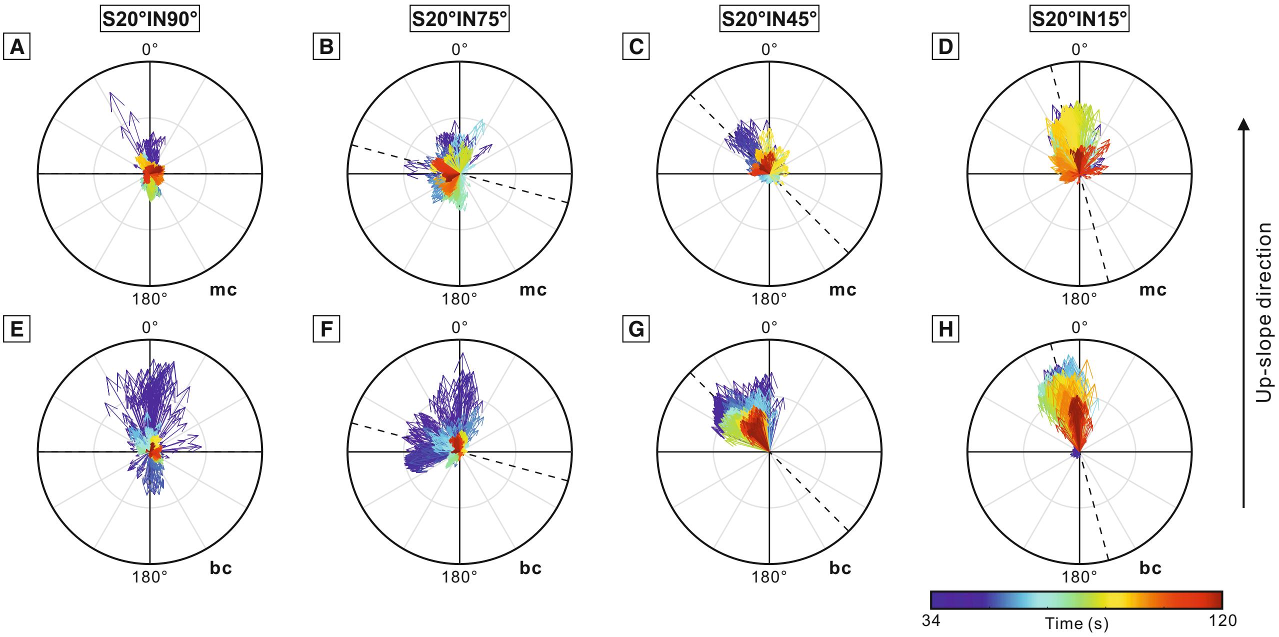

Fig. 12. Compass plots illustrating the temporal variability of the flow velocity vector (projected in the horizontal basin-floor) of the current recorded at 0.01 m above the basin floor and/or the slope surface within the quasi-steady phase (34–120 s) in Experiments S20°IN90° (A, E), S20°IN75° (B, F), S20°IN45° (C, G) and S20°IN15° (D, H). 'bc' denotes the measurements at the base of slope and 'mc' denotes the measurements at the central 'flow front' position (ADV3 in Fig. 1). In each compass plot, the arrow length denotes the velocity magnitude, and the direction denotes the velocity direction relative to the basin. Each arrow is colour coded as time. Black dashed line indicates the slope orientation. For presentation, in each compass plot, the original 100 Hz ADV velocity data are decimated to 10 Hz. See Fig. 11 for the legend of this figure.

10–20% of that of the quasi-steady flow (Fig. 14).

Results indicate that within a near frontal experimental configuration (S20°IN75° and S20°IN90°; Fig. 14G–K), the near-bed velocity vectors on the slope surface tend to be dominated by a reflected downslope flow direction with a nearly orthogonal angle to the topographic slope orientation. This is likely because when the dilute flow declines higher up on the slope surface, gravity starts to dominate and therefore the flow collapses orthogonal to the slope. In a highly oblique or oblique experimental configuration (S20°IN15°; S20°IN45°; Fig. 14A–F), the near-bed flow directions during the waning phase are more variable, with flows showing a high degree of radial spreading in places (Fig. 14B, E and F), and mean flow angles in the range of *ca* 30–45° relative to the slope strike or orientation. This is attributed to the input flow not riding up the slope as high, and therefore, gravity having a minor influence relative to the basinward flow momentum.

Summary of flow processes

Effect of containing topographic orientation on flow behaviour

Flow visualization (Videos 1–3) and quantitative velocity data (e.g. Fig. 5) demonstrate that flows that are highly oblique to the containing slope are characterized by: (i) limited lateral flow expansion on the slope surface, (ii) limited flow decoupling and stripping and (iii) stronger flow deflection than flow reflection in the basal part of the flow (Fig. 15). In contrast, flows with a high flow incidence angle configuration, and therefore a high degree of topographic containment, promote the development of: (i) a high degree of flow divergence on the slope surface; (ii) a high degree of flow decoupling and stripping; and (iii) stronger flow reflection than flow deflection.

The weaker basal flow reversal (i.e. weaker flow reflection) with a higher obliquity of flow to the slope is also supported by the longitudinal velocity time series measurements of the flows recorded at the base of the slope (Fig. 5).

13653091, 0, Downloaded from https://onlinelibrary.wiley.com/doi/10.1111/sed.70032 by Schweizerische Akademie Der, Wiley Online Library on [20/07/2025]. See the Terms and Conditions (https://onlinelibrary.wiley.com/terms-and-conditions) on Wiley Online Library for rules of use; OA articles are governed by the applicable Creative Commons License

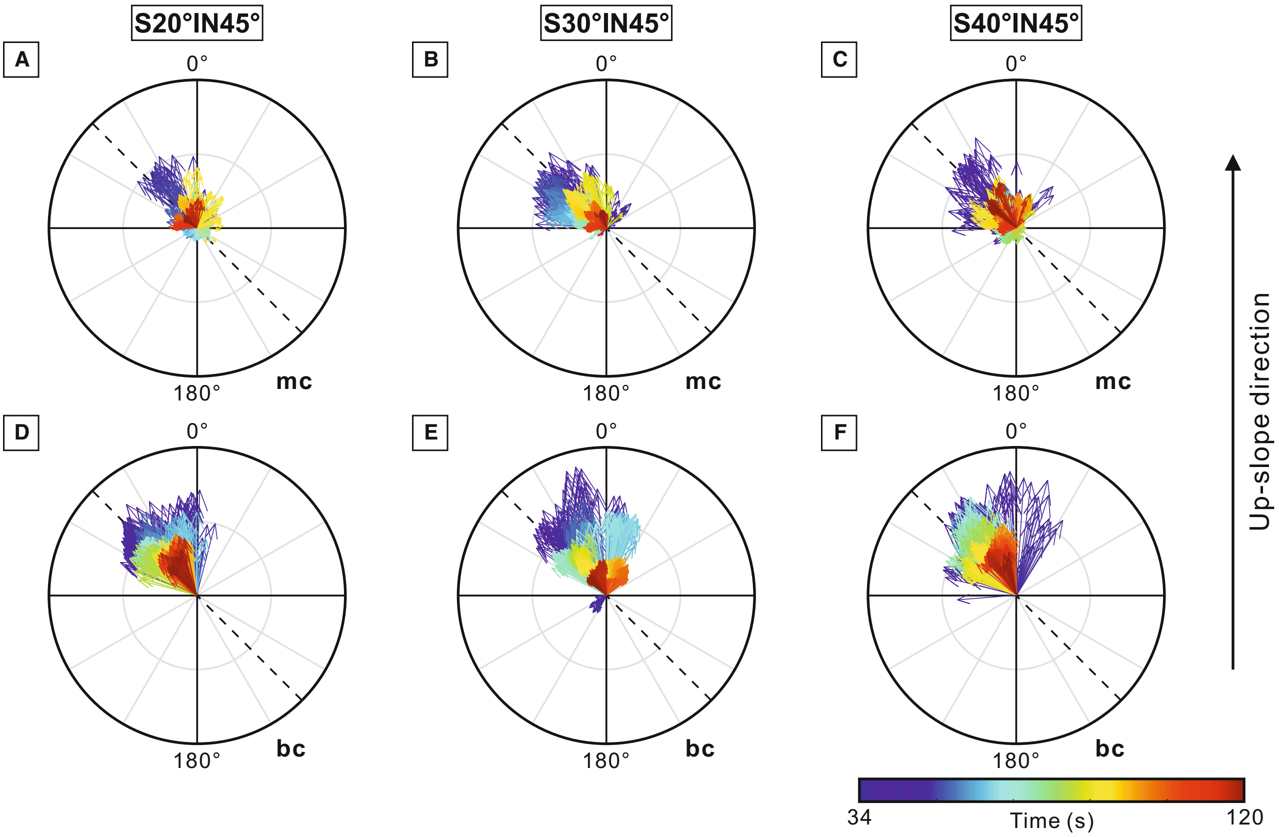

Fig. 13. Compass plots illustrating the temporal variability of the flow velocity vector (projected in the horizontal basin-floor) of the current within the quasi-steady phase (34–120 s) recorded at 0.01 m above the basin floor and/or the slope surface in Experiments S20°IN45° (A, D), S30°IN45° (B, E) and S40°IN45° (C, F). 'bc' denotes the measurements at the base of slope and 'mc' denotes the measurements at the central 'flow front' position (ADV3 in Fig. 1). In each compass plot, the arrow length denotes the velocity magnitude, and the direction denotes the velocity direction relative to the basin. Each arrow is colour coded as time. Black dashed line indicates the slope orientation. For presentation, in each compass plot, the original 100 Hz ADV velocity data are decimated to 10 Hz. See Fig. 11 for the legend of this figure.

These illustrate a marked decrease in the magnitude of the maximum velocity $U_{\max}$ and a much greater number and shorter time duration of velocity reversals. In addition to these reversals, there are also a range of other smaller scale flow fluctuations across a spectrum of frequencies.

Effect of containing slope angle on flow behaviour

Flows interacting with steeper slopes are typically associated with: (i) less flow divergence on the slope surface; (ii) limited flow decoupling and stripping; and (iii) increased flow deflection relative to flow reflection of the basal part of the flow (Videos 1, 4; Fig. 6). Across different slope gradients, the magnitude of the maximum velocity shows minimal difference, suggesting that the influence of slope gradient on flow reflection is weaker than that of the angle of incidence. However, flows with higher slope gradients are associated with more and shorter pulses (velocity reversals) (Fig. 6).

In summary, the experimental results from a simple planar containing slope demonstrate how the dominant flow processes transition from lateral divergence-dominated, through reflection-dominated to deflection-dominated as the flow incidence angle varies from 90° to 15° and the slope gradient changes from 20° to 40° (Fig. 15). Crucially, the incidence angle of the current to the slope exerts a stronger control on the relative strength of flow deflection and flow reflection, whereas the slope gradient more strongly affects

© 2025 The Author(s). *Sedimentology* published by John Wiley & Sons Ltd on behalf of International Association of Sedimentologists, *Sedimentology*

13653091, 0, Downloaded from https://onlinelibrary.wiley.com/doi/10.1111/sed.70032 by Schweizerische Akademie Der, Wiley Online Library on [20/07/2025]. See the Terms and Conditions (https://onlinelibrary.wiley.com/terms-and-conditions) on Wiley Online Library for rules of use; OA articles are governed by the applicable Creative Commons License

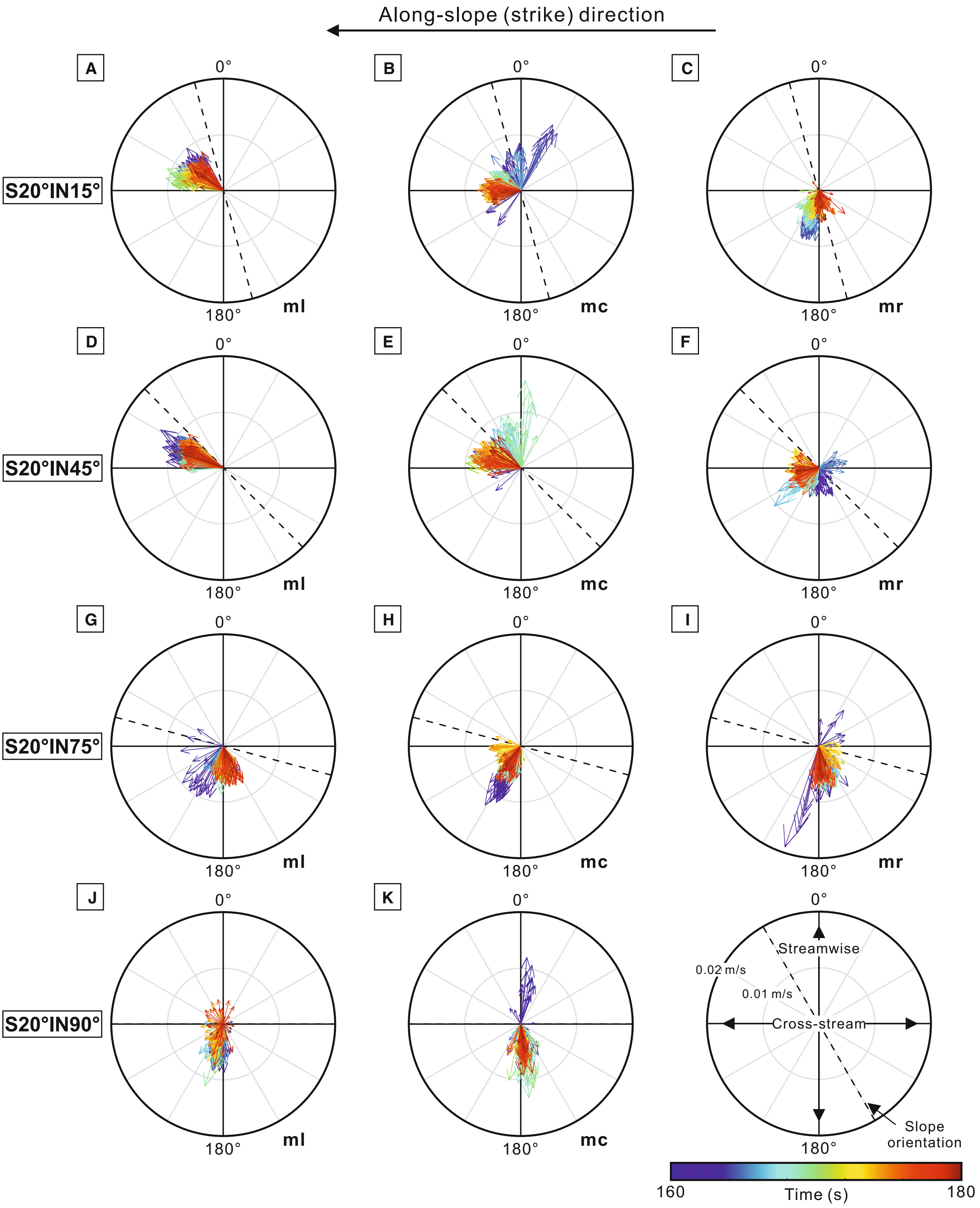

© 2025 The Author(s). *Sedimentology* published by John Wiley & Sons Ltd on behalf of International Association of Sedimentologists, *Sedimentology*

13653091, 0, Downloaded from https://onlinelibrary.wiley.com/doi/10.1111/sed.70032 by Schweizerische Akademie Der, Wiley Online Library on [20/07/2025]. See the Terms and Conditions (https://onlinelibrary.wiley.com/terms-and-conditions) on Wiley Online Library for rules of use; OA articles are governed by the applicable Creative Commons License

Fig. 14. Compass plots illustrating the temporal variability of the flow velocity vector (projected in the horizontal basin-floor) of the current within the waning phase (160–180 s) recorded at 0.01 m above the slope surface in Experiments S20°IN15° (A–C), S20°IN45° (D–F), S20°IN75° (G–I) and S20°IN90° (J, K). 'ml', 'mc' and 'mr' denote the measurements at the left, central and right 'flow front' positions (in the flow direction), respectively (ADV4, ADV3 and ADV2 in Fig. 1). In each compass plot, the arrow length denotes the velocity magnitude, and the direction denotes the velocity direction relative to the basin. Each arrow is colour coded as time. Black dashed line indicates the slope orientation. For presentation, in each compass plot, the original 100 Hz ADV velocity data are decimated to 10 Hz. Note the different velocity scale for the arrows relative to Figs 11–13. Note that the vectors from panel C are anomalous, as they represent drainage of the waning flow over the right hand (upstream) lateral edge of the ramp.

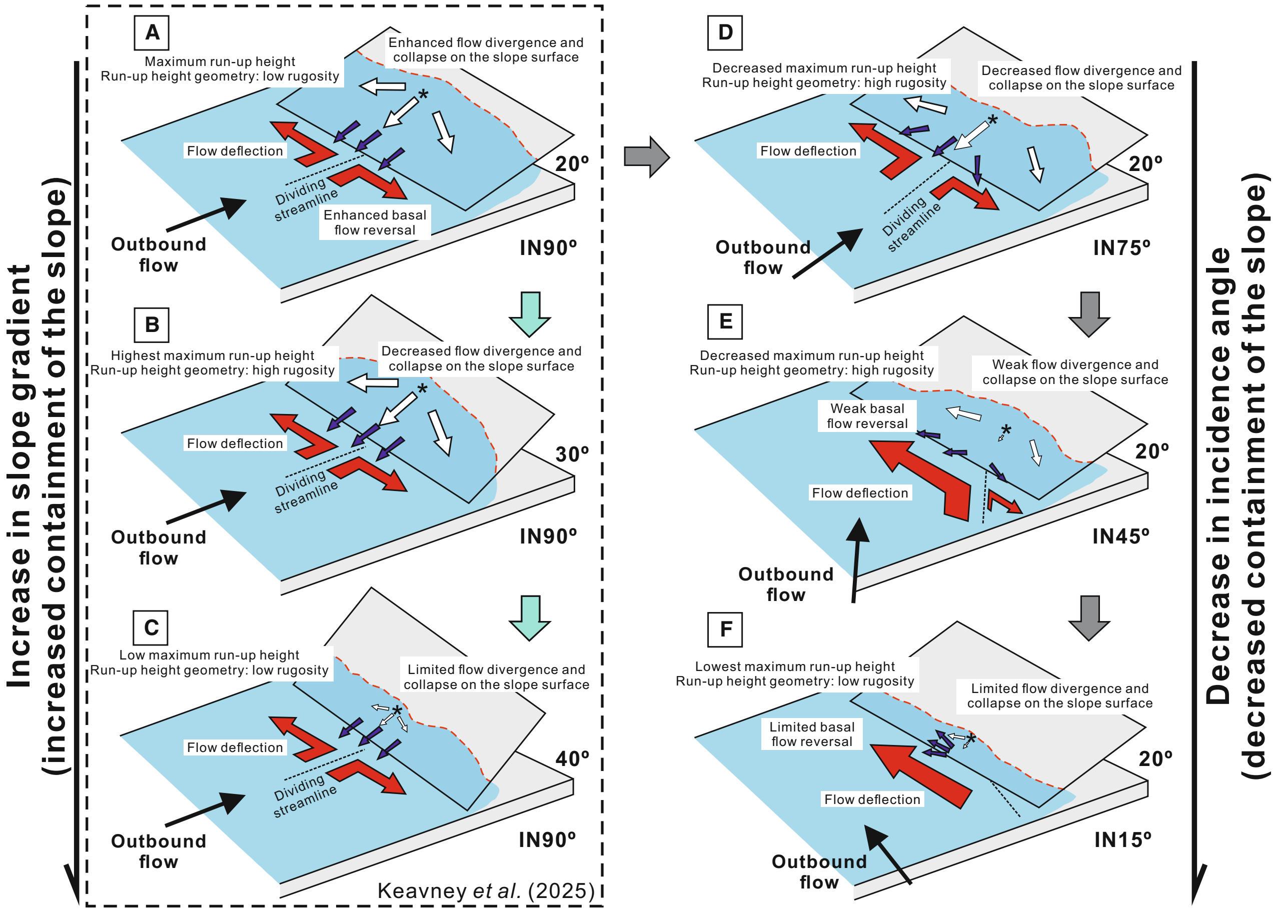

Fig. 15. Schematic diagram illustrating the influence of flow incidence angle on the topographic slope (A, D–F) and slope gradient (A–C) on the general flow behaviour of steady input density currents. Panels A–C are modified from Keavney *et al.* (2025) to help comparison. The light blue indicates the area which is covered by the flow. The black arrow represents the outbound flow direction. Red arrows indicate flow deflection. Dark blue arrows at the base of the slope indicate flow reflection and deflection directions at the base of the ramp; arrows do not show magnitude. White arrows on the slope surface indicate the reflected and deflected flows on the slope surface, the size of which is a schematic guide to the relative flow strength. The central reflection arrows in panels A-F, highlighted by asterisks, indicate the transient nature of this orthogonal flow reflection, especially in panels E and F, where these orthogonal reflected flows are very rarely seen, and velocities are low (see details in Fig. 12A–D). Dividing streamline (better termed as the dividing stream plane; cf. Baines, 1995), is shown as a dashed line in each topographic configuration and is the critical plane within the flow whereby the left and right side of the fluid particles move in opposing directions along the base of the ramp.

13653091, 0, Downloaded from https://onlinelibrary.wiley.com/doi/10.1111/sed.70032 by Schweizerische Akademie Der, Wiley Online Library on [20/07/2025]. See the Terms and Conditions (https://onlinelibrary.wiley.com/terms-and-conditions) on Wiley Online Library for rules of use; OA articles are governed by the applicable Creative Commons License

the degree of flow divergence, flow decoupling and stripping on the slope surface.

DISCUSSION

Spatial variation of combined flows on slopes

Combined flows in deep-water settings are hypothesized to form as turbidity currents interact with seafloor topography (Kneller *et al.*, 1991; Edwards *et al.*, 1994; Tinterri, 2011; Patacci *et al.*, 2015; Tinterri *et al.*, 2016, 2022; Keavney *et al.*, 2025). The experiments herein (Fig. 4, Figs 11–13 and Videos 1–4) support the generation of combined flow in 3D unconfined density current above a topographic slope, consistent with Keavney *et al.* (2025) for the 90° incidence angle case. The initial unidirectional parental flow transforms upon incidence with the slope into a multidirectional parental flow on the slope surface, which then collapses downslope (Fig. 15 and Videos 1–4). The resultant combined flow is a combination of the multidirectional flow up the ramp and the reflected flow downslope. This study extends the work on orthogonal incidence angles (Keavney *et al.*, 2025) and demonstrates the generation of combined flows across a wide set of topographic slope configurations.

Crucially, this work (Figs 11–13) presents a broad range of multidirectional combined flows, the unidirectional component of which varies markedly with different locations on a single containing slope, as well as with different topographic slope configurations (both orientation and slope gradient). Above a single planar slope, as the density current interacts with the topography, the initial unidirectional parental flow is transformed into a strongly multidirectional flow high up on the slope. Therefore, more radial dispersal patterns in flow direction distribution are noted for the flows documented at the ‘flow front’ position compared to those recorded at the base of slope (Figs 11 and 12A–D versus Fig. 12E–H). A narrower spread in flow directions along the slope (Fig. 11A–C) is likely because the reversing flow at the downstream position tends to collapse downslope and converge with the basal flow running parallel to the slope, likely leading to the establishment of combined flow with a unidirectional component oriented parallel to the slope orientation. In a low flow incidence angle setting, the increased unidirectional component of the flow recorded at the central ‘flow front’ position high up on the slope (Fig. 12A–D) could be explained by an enhanced influence of flow deflection running parallel to the slope on the flow directions; this is due to a decrease in topographic containment from a near frontal to a highly oblique topographic slope setting (Fig. 15F).

This work demonstrates that multiple types of complex multidirectional combined flows can be generated above planar topographic slopes by changing the orientation or slope angle of the containing topographic slope. The interaction of density currents with non-planar seafloor topography and unsteady flows in field examples would favour the establishment of even more complex patterns of combined flows above slopes.

Absence of observable internal waves

In all ramp experiments, no well-defined internal wave-like features are observed visually (Videos 1–4). Additionally, repetitive, regular coherent structures with similarities to putative internal waves (Marshall *et al.*, 2021, 2023) are not shown in the streamlines and power spectral analysis of the gravity currents over the height interval covered by the ADV (Figs 9, 10 and S1). The lack of observable internal waves may be due to three key factors: (i) the order(s) of magnitude lower density of the flows compared with previous experiments (e.g. Kneller *et al.*, 1991; Kneller, 1995), which produce weaker reflections and instead enable flows to expand and deflect on the slope; (ii) the low incoming Froude numbers, which limit the potential for reflected flows to become supercritical and produce hydraulic jumps, and thus to form bores that can translate into internal waves (cf. Pantin & Leeder, 1987; Edwards *et al.*, 1994); and (iii) the complex, three-dimensional flow fields due to flow deflection and reflection, which lead to combined flows that vary rapidly both spatially and temporally. It is postulated herein that the complex 3D flow field likely disrupts the development of discrete two-dimensional internal waves. Such spatial and temporal variations of three-dimensional flow represent very different conditions to those in 2D experiments in narrow channels where trains of internal waves have been observed to form (e.g. Pantin & Leeder, 1987; Edwards *et al.*, 1994; Patacci *et al.*, 2015). This said, it is noted that quantitative data at the flow-ambient interface were not collected, albeit waves on this interface would be expected to be seen visually, as observed

13653091, 0, Downloaded from https://onlinelibrary.wiley.com/doi/10.1111/sed.70032 by Schweizerische Akademie Der, Wiley Online Library on [20/07/2025]. See the Terms and Conditions (https://onlinelibrary.wiley.com/terms-and-conditions) on Wiley Online Library for rules of use; OA articles are governed by the applicable Creative Commons License

clearly in previous experiments (e.g. Kneller *et al.*, 1991; Kneller, 1995).

Velocity pulsation on slopes

The input flow in the experiments is quasi-steady in nature (Table 1). However, whilst internal waves are not identified, distinct temporal velocity pulsing or velocity unsteadiness, in the basal part of the flows is recorded in all experimental configurations, both at the base of, and on the topographic slope, as measured along the channel-basin centreline (Figs 5–8). This velocity pulsing is generated by the repeated fluctuations of the 'flow front', with periodic rises and collapses of fluid up and down the slope. In turn, the nature of the velocity pulsing in terms of velocity amplitude and frequency varies as a function of incidence angle and slope angle (Fig. 16). This mechanism for velocity pulsing is therefore tied to slopes and the base of slopes but will likely not propagate much further into the basin. Slopes have previously been associated with the generation of velocity pulsing, but this has either been in the form of solitons and internal waves (Kneller *et al.*, 1991, 1997; Edwards *et al.*, 1994; Kneller, 1995; Patacci *et al.*, 2015), the generation of true oscillatory flows (Tinterri, 2011; Tinterri & Muzzi Magalhaes, 2011) or due to postulated pulses within the input flow (Kneller & McCaffrey, 1999). The present experiments do not show evidence for the generation of oscillatory flows, with the pulsation related to movement of fluid up and down the slope, rather than propagation of a wave through the medium. Similarly, there is no clear visual or quantitative evidence for the development of solitons or internal waves in the present experiments (see *Absence of observable internal waves* subsection).

This mechanism for velocity pulsing on slopes might potentially be combined with other velocity pulsing mechanisms intrinsic to flows such as Kelvin–Helmholtz or Holmboe waves (Kostaschuk *et al.*, 2018), or internal waves (Marshall *et al.*, 2021, 2023). Such pulsing mechanisms are likely at a higher frequency (Kostaschuk *et al.*, 2018), and thus subsidiary to the slope-induced pulsing. More complex velocity pulsation may be possible where the flows themselves are driven, or where stratified flows are perturbed by externally induced pulsation, such as Rayleigh–Taylor instabilities generated in some plunging flows (Best *et al.*, 2005; Dai, 2008; Kostaschuk *et al.*, 2018), or via other external drivers such as roll waves, storms, wind- or tide-driven circulation, river discharge events or cyclic slope failure (e.g. Syvitski & Hein, 1991; Kneller & McCaffrey, 1999; Ogston & Sternberg, 1999; Ogston *et al.*, 2000; Li *et al.*, 2001; Wright *et al.*, 2002).

Spatial distribution of combined flow bedforms on slopes

Combined flow sedimentary structures, including small- to medium-scale biconvex ripples with internal sigmoidal-cross laminae and hummock-like bedforms, have been identified in deep-water turbidites at outcrop (e.g. Marjanac, 1990; Haughton, 1994; Remacha *et al.*, 2005; Mulder *et al.*, 2009; Tinterri, 2011; Tinterri *et al.*, 2016, 2022; Hofstra *et al.*, 2018; Martínez-Doñate *et al.*, 2021; Privat *et al.*, 2021; Taylor *et al.*, 2024). The formation of these sedimentary structures has been typically hypothesized to be linked to the generation of combined flows by the superposition of a unidirectional parental turbidity current with an oscillatory component formed by internal waves generated by reflection against a topographic slope (Tinterri, 2011; Tinterri *et al.*, 2016, 2022; see also Kneller *et al.*, 1991; Edwards *et al.*, 1994; Haughton, 1994). Such models depend in part on the basis of observations of reflected bore-generated internal waves in 2D or qualitative 3D reflected density current experiments (e.g. Kneller *et al.*, 1991; Edwards *et al.*, 1994). Nevertheless, the present experimental work documents the generation of complex, multidirectional combined flows on the slope surface when unconfined gravity currents interact with all oblique topographic slope configurations (Figs 11–13; Videos 1–4). This is at odds with these previous models and instead supports the model for the formation of hummock-like bedforms through combined flows on slopes as proposed by Keavney *et al.* (2025). Herein, this model of Keavney *et al.* (2025) is demonstrated to be applicable to a wider range of topographic configurations. Hummock-like bedforms form during relatively high sediment fallout rates (Tinterri, 2011) when flows decelerate upon incidence with the slope and under combined flow conditions with a radial dispersal pattern (Keavney *et al.*, 2025). Sigmoidal bedforms form during relatively lower sediment fallout rates (Tinterri, 2011) under combined flows with a radial dispersal pattern but a strong unidirectional component.

© 2025 The Author(s). *Sedimentology* published by John Wiley & Sons Ltd on behalf of International Association of Sedimentologists, *Sedimentology*

13653091, 0, Downloaded from https://onlinelibrary.wiley.com/doi/10.1111/sed.70032 by Schweizerische Akademie Der, Wiley Online Library on [20/07/2025]. See the Terms and Conditions (https://onlinelibrary.wiley.com/terms-and-conditions) on Wiley Online Library for rules of use; OA articles are governed by the applicable Creative Commons License

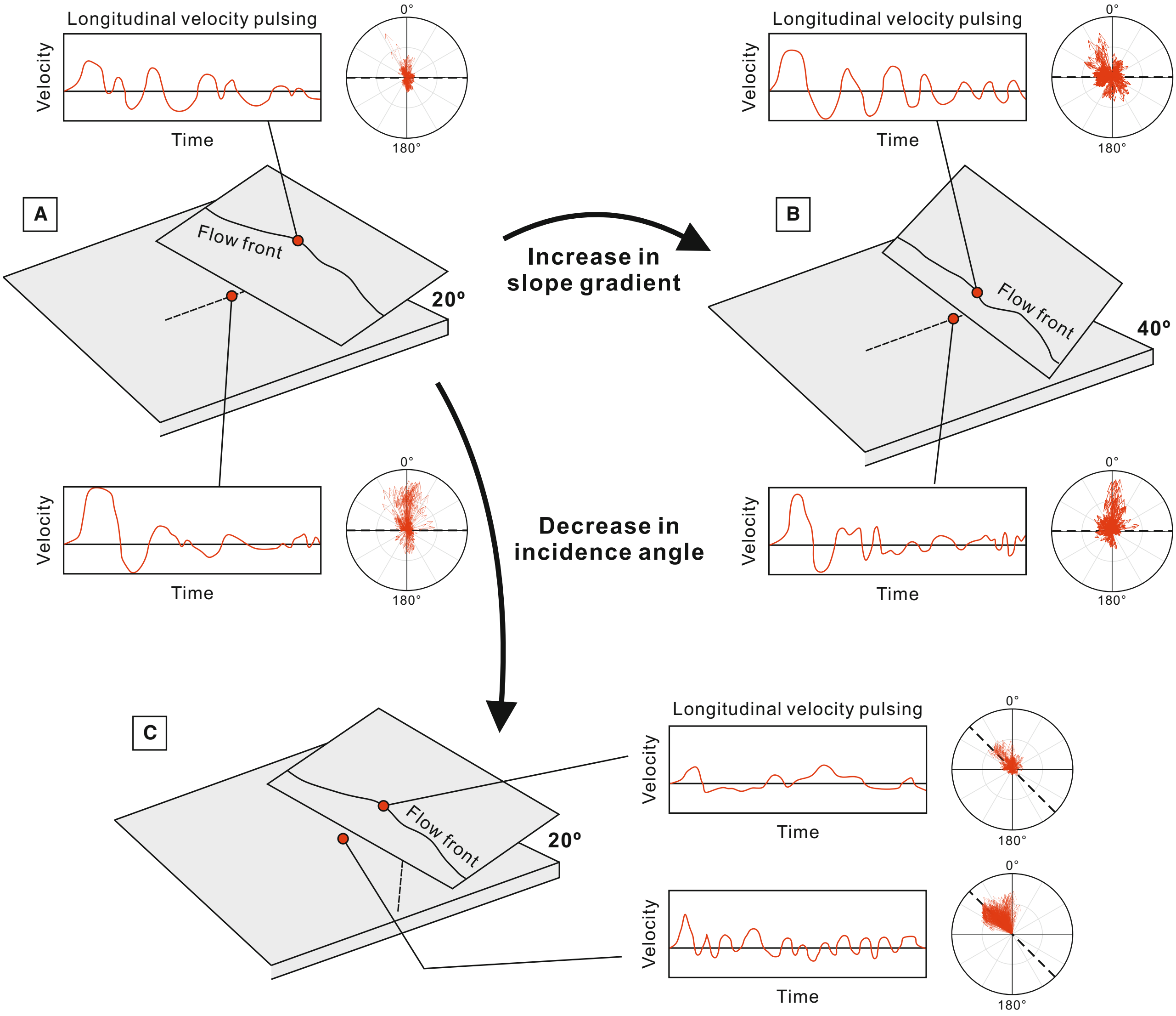

Fig. 16. Schematic diagram illustrating the influence of different containing topographic configurations (orientation and slope gradient) on the temporal pulsing pattern of the longitudinal velocity and temporal variability in the velocity vector (based on longitudinal and cross-stream velocity). As the incidence angle decreases (A and C), velocity pulsing recorded at the base of the slope is characterized by: (i) a marked decrease in the magnitude of the maximum velocity $U_{\max}$, (ii) a greater number of velocity pulses and (iii) a much shorter duration of each pulse. In cases with a steeper slope gradient (A and B), a subtle decrease in $U_{\max}$, and relatively more and shorter velocity pulses are recorded. Velocity pulsing recorded at the 'flow front' position in experiments with a low flow incidence angle to the slope (A and C) is characterized by a more irregular, non-periodic nature, comparatively fewer and longer velocity pulses. There is negligible difference in $U_{\max}$, and relatively more and shorter velocity pulses for cases with a steeper slope gradient (A and B).

As the flow incidence angle decreases, the enhanced dominance of flow deflection versus reflection (Fig. 15) is documented to result in a progressive increase in the unidirectional component of the generated combined flows high up on the slope (Fig. 12A–D). This in turn may lead to the deposition of hummock-like bedforms characterized by an increased degree of anisotropy (isotropic to strongly anisotropic) or even sigmoidal bedforms when the unidirectional component is very strong. Slope gradient will only have a limited effect on the degree of anisotropy due to the subtle difference in the types of the generated combined flow (Fig. 13A–C). Consequently, the degree of anisotropy in hummock-like bedforms is a good indicator of

13653091, 0, Downloaded from https://onlinelibrary.wiley.com/doi/10.1111/sed.70032 by Schweizerische Akademie Der, Wiley Online Library on [20/07/2025]. See the Terms and Conditions (https://onlinelibrary.wiley.com/terms-and-conditions) on Wiley Online Library for rules of use; OA articles are governed by the applicable Creative Commons License

the flow incidence angle to the topographic slope, rather than the slope gradient.

Revisiting the paradigm of flow deflection and reflection

The existing paradigm

The prevailing paradigm for sediment gravity flow interaction with planar topographic slopes is that there is a reflected component that is always orthogonal to the topographic slope irrespective of the incidence angle of the flow (Kneller *et al.*, 1991; Kneller, 1995; Kneller & McCaffrey, 1999; Fig. 17A; note though that the single experiment in Haughton, 1994 is slightly anomalous). This leads to a model where sole marks, representing basal conditions, can be at high angles to ripple directions, within the same bed; for flows parallel with containing topography, the angle is 90° (Kneller *et al.*, 1991; Kneller, 1995; Fig. 17B). In turn, the reflections are linked to internal waves (Pantin & Leeder, 1987; Kneller *et al.*, 1991; Edwards *et al.*, 1994; Haughton, 1994; Kneller, 1995), or to externally driven pulses in the input flow producing periods dominated by orthogonal reflection (Kneller & McCaffrey, 1999). However, the experiments herein do not support this model with a notable absence of downslope reflection at more oblique incident angles (15° and 45°) during the main body of the flow (Figs 12 and 13, Video 3), along with a lack of evidence for internal waves (see *Absence of observable internal waves* subsection). In the present experiments, the dominant flow processes transition from lateral divergence-dominated, through reflection-dominated, to deflection-dominated as the flow incidence angle varies from 90° to 15° and the slope gradient changes from 20° to 40° (Fig. 15).

The existing paradigm was developed from qualitative 3D experiments against oblique, and parallel to flow, containing slopes (Kneller *et al.*, 1991; Kneller, 1995), which therefore appear paradoxical compared to the present experiments. The key to this conundrum is that the previous experiments were run in a very small tank, 1 m by 1 m in planform, and consequently, flows were in a strongly expansional phase having exited the inlet channel when they interacted with the containing slope (Kneller *et al.*, 1991, Fig. 17C). Hence, the local flow direction relative to the slope was approximately orthogonal (Kneller *et al.*, 1991, Fig. 17C; Kneller, 1995, his fig. 13). Consequently, the slopes were not oblique relative to the local flow direction of the impinging flow, and therefore, the resulting reflections were essentially orthogonal to the slope, and thus comparable with 2D experiments on orthogonal slopes (e.g. Edwards *et al.*, 1994).

The previous 3D experiments (Kneller *et al.*, 1991; Kneller, 1995) did generate clear internal waves, as also observed for 2D slopes (Edwards *et al.*, 1994), which were not observed in the present experiments. Key to this difference may be the orders of magnitude differences in the density of the impinging flows. In the

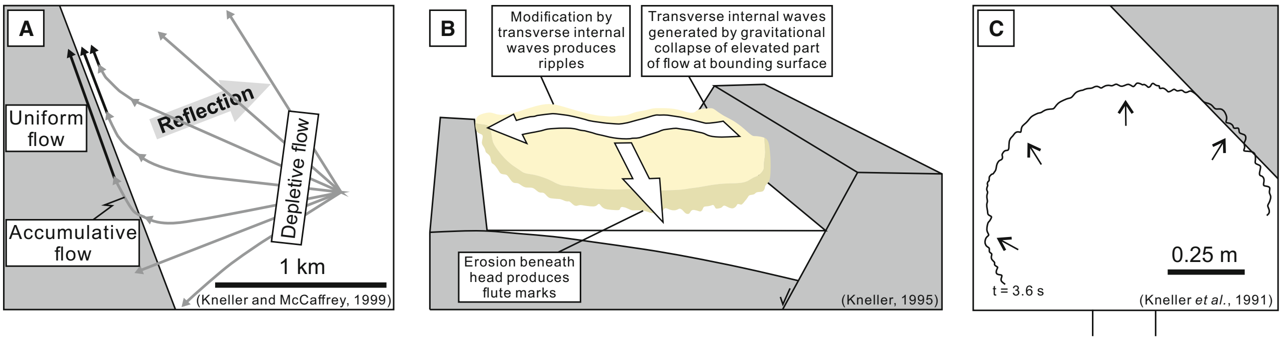

Fig. 17. Existing process models for flow deflection and reflection when sediment gravity flows encounter a topographic slope (A and B) and for the resulting relationship between sole mark and ripple directions (B). In these models, there is always a component of flow that is reflected orthogonal to the topographic slope, irrespective of the incidence angle of the flow against the slope. Ripples are formed as the product of internal waves travelling on the upper interface of the gravity current, as shown in (B). (C) Small-scale experiment of Kneller *et al.* (1991) as seen in planform, showing expanding flow interacting with a slope (marked in grey). Whilst the slope is oblique relative to the axial flow direction of the current, due to expansion the local flow direction is orthogonal to the slope at the point where the flow interacts with the slope (redrawn from Kneller *et al.*, 1991).

© 2025 The Author(s). *Sedimentology* published by John Wiley & Sons Ltd on behalf of
International Association of Sedimentologists, *Sedimentology*

13653091, 0, Downloaded from https://onlinelibrary.wiley.com/doi/10.1111/sed.70032 by Schweizerische Akademie Der, Wiley Online Library on [20/07/2025]. See the Terms and Conditions (https://onlinelibrary.wiley.com/terms-and-conditions) on Wiley Online Library for rules of use; OA articles are governed by the applicable Creative Commons License

present study, flows were dilute (*ca* 0.3% density difference), in contrast to 6.7–12.8% density differences reported in Kneller *et al.* (1991), and 3% in Kneller (1995). Note that these are initial values for the Kneller *et al.* (1991) and Kneller (1995) cases; however, the small tank size limited the time for entrainment and dilution prior to impacting the slope. Flows that are 1–2 orders of magnitude greater in density will be prone to far stronger flow reflection and will lack the run-up heights and more complex interaction with slopes observed herein. Whilst the bulk (depth-averaged) flow density of natural turbidity currents remains poorly known, the best estimates range from <0.1% to *ca* 0.2% (Konsoer *et al.*, 2013; Simmons *et al.*, 2020), comparable to natural saline-driven density currents (*ca* 0.1–0.2%; Sumner *et al.*, 2014; Azpiroz-Zabala *et al.*, 2024). Consequently, the present experiments are far more comparable to those low-density turbidity currents estimated from natural systems. However, this comparative exercise does suggest that flow density is a key variable that requires further assessment.

The model of ripple formation from internal waves is itself problematic. This is because the internal waves are postulated to form at the upper interface of the turbidity current in the original model (Kneller *et al.*, 1991; Kneller, 1995). Given that natural unconfined or partially confined turbidity currents can be metres to tens of metres in thickness (e.g. Stevenson *et al.*, 2013; Lintern *et al.*, 2016; Hill & Lintern, 2022), then the internal waves would need to be large and of the order of the flow depth, to be able to penetrate to the bed. Furthermore, the internal-wave driven model of Kneller (1995; Fig. 17B) has both the axial flow and the ripple generating transverse flows present at the same time. However, there is a temporal gap between the formation of the sole marks and the ripples, particularly as there may be a substantial time gap between the cutting of the sole marks and the deposition of the immediately overlying sediment (Peakall *et al.*, 2020; Baas *et al.*, 2021). Furthermore, the ripples in the Bouma C division are typically formed right at the end of sand deposition. Thus, it could be hypothesized that the ripples may reflect the waning phase of the flow where the incident flow declines, leaving gravity to dominate, with flows collapsing orthogonal to the slope. For high incidence angle slopes (75° and 90°), the present experiments show that waning flows on slopes are orthogonal (Fig. 14G–K). In contrast, highly oblique slopes (15°) and oblique slopes (45°) show far greater variability in flow directions in the waning flows (Fig. 14A–F), with flows showing a high degree of radial spreading in places (Fig. 14B), and mean flow angles in the range of *ca* 30–45° relative to the slope strike or orientation, rather than orthogonal (Fig. 14A–C). So even waning flows in highly oblique systems are not predominantly orthogonal to slopes as suggested in the existing model (Kneller *et al.*, 1991; Kneller, 1995; Kneller & McCaffrey, 1999).

The conundrum of palaeocurrent data in elongate basins

A further conundrum is that palaeocurrent data in elongate basins typically show high angles between basin axial sole structures and basin transverse ripples in flows that were postulated to be broadly parallel to slopes (e.g. Cope, 1959; Craig & Walton, 1962; Prentice, 1962; Kelling, 1964; Seilacher & Meischner, 1965; Scott, 1967; Kneller *et al.*, 1991; Pickering *et al.*, 1992; Smith & Anketell, 1992), with Kneller *et al.* (1991) showing a peak in angular discordance between 60° and 90°. These field data are thus in agreement with the Kneller *et al.* (1991) model of orthogonal reflection. Given, the experiments herein demonstrate that orthogonal reflection is not universal, as previously postulated (Kneller *et al.*, 1991), and does not occur under highly oblique incidence angles, why do field examples interpreted to have flows broadly parallel to slopes appear to show orthogonal flow reflection? In order to address this conundrum, a flow visualization experiment was undertaken of a flow whose axis is parallel to a topographic ramp; the ramp was positioned with its upstream edge at 2 m from the channel mouth and base of it on the channel-basin centreline; the run time and basic set up were the same as the other experiments (Fig. 18). The visualization (Fig. 18 and Video 5) shows a flow that produces a 'flow front' that oscillates up and down the topographic ramp, with return (down-slope) movement orthogonal to the slope. So why do 'flow fronts' form on a slope parallel to the flow? Firstly, the flow was still spreading and thus diverging slightly as it interacted with the slope (Video 5). The resulting net lateral flow towards the slope leads to fluid being initially pushed up the slope. Secondly, the head of the flow is higher than the body of the flow (Video 5). Consequently, the head travels further up the slope than the subsequent body of the flow, leading to a net drawdown of fluid after

13653091, 0, Downloaded from https://onlinelibrary.wiley.com/doi/10.1111/sed.70032 by Schweizerische Akademie Der, Wiley Online Library on [20/07/2025]. See the Terms and Conditions (https://onlinelibrary.wiley.com/terms-and-conditions) on Wiley Online Library for rules of use; OA articles are governed by the applicable Creative Commons License

the head passes (Video 5). The combination of these processes leads to flow reversal orthogonal to the slope. The interaction of the return flow with the outbound flow, in turn initiates an oscillation up and down the slope. Such an interaction is to be expected in sedimentary basins, as: (i) flows may still be spreading when they interact with basin margins (or intra-basinal topography) that are broadly parallel to the axis of the basin; (ii) basin-margin (or intra-basinal) slopes will not be perfectly parallel for any substantial distance relative to basin length, and small changes to slope orientation will lead to local flow divergence; (iii) flow heads are different heights to the body in real-world flows (e.g. Komar, 1972); and (iv) as the flow wanes, the height of the flow body will progressively decline, in turn setting up (or enhancing) an oscillation orthogonal to the slope. This latter effect may be key, as the formation of ripples is related to a relatively late phase as the flow decelerates. The oscillations and thus the ‘flow fronts’ are observed because they rise above the height of the main flow (Video 5), and thus in their upper parts collapses are dominated by gravitational force. In their lowermost parts, there is a progressive interaction with the axial flow, but there is a significant region with net flows at high angles to the slope (Video 5). These observations of orthogonal flow down much of the slope, and high angle flow relative to the slope at lower elevations, thus provide an explanation for the palaeocurrent data from elongate basin-fills.

A new model for flow deflection and reflection

Flows that are at very high angles to topographic slopes produce orthogonal reflections down the slope. As flows become more oblique, they are deflected rather than reflected, and do not exhibit orthogonal reflections, even in the case of waning flows that might be expected to generate ripples. Once flows become broadly parallel to topographic slopes, spatial changes in topographic orientation, temporal changes in flow height or flow divergence if the flow is still expanding lead to up-slope and down-slope flow oscillations orthogonal to the bounding topographic slope. These orthogonal flow directions relative to the slope are in agreement with the very high angles of ripples relative to sole marks from elongate basin-fills. This new model of flow reflection and deflection (Figs 15 and 19A) shows that the incidence angle of the flow against the slope is critical. Flows do not universally reflect orthogonally off planar topographic slopes as believed for the past three decades (Kneller *et al.*, 1991; Kneller & McCaffrey, 1999). The mechanics observed herein are also radically different to that proposed in the current paradigm. Ripples are formed on slopes and close to the base of slopes by flows moving down the slope, in many cases during the waning of flows, rather than being the product of internal waves travelling on the upper interface of the gravity current (Kneller *et al.*, 1991; Kneller, 1995; Fig. 19A–D). The present model suggests that palaeocurrents showing high angles between sole marks and ripples are formed on, or close to, slopes in contrast to the model of Kneller (1995; Fig. 17B) that shows such relationships occurring across entire basins.

Implications for natural sediment-laden flows and their deposits

In keeping with most previous experiments on gravity currents interacting with planar slopes, the present work utilized saline flows. However, natural turbidity currents are typically associated with increased stratification, particularly during flow deceleration and deposition as are likely to occur as flows encounter topography (Menard & Ludwick, 1951; Gladstone *et al.*, 2004; Amy *et al.*, 2005; Dorrell *et al.*, 2014; Peakall & Sumner, 2015). Enhanced stratification relative to the experiments has been argued to lead to: increased density decoupling and run-up of the more dilute parts of the flow; and a greater potential for the formation of internal waves (Keavney *et al.*, 2025). Internal waves in gravity currents have been associated with sharp density variations (e.g. Kneller *et al.*, 1991; Patacci *et al.*, 2015; Dorrell *et al.*, 2019); however, little is known about their interaction with pronounced continuous stratification as would likely occur in strongly depositional systems (Peakall & Sumner, 2015). Furthermore, the present study postulates that strongly three-dimensional flow fields of unconfined flows on slopes, and the rapid variations in these temporally and spatially, likely act to restrict the initial generation of internal waves. It is difficult to know *a priori* how increased stratification will affect both: (i) the propensity for internal wave generation if considered purely in a two-dimensional flow, and (ii) the changes to the three-dimensional flow fields and in turn their influence on internal wave generation. These areas offer avenues for future investigation. A

© 2025 The Author(s). *Sedimentology* published by John Wiley & Sons Ltd on behalf of

13653091, 0, Downloaded from https://onlinelibrary.wiley.com/doi/10.1111/sed.70032 by Schweizerische Akademie Der, Wiley Online Library on [20/07/2025]. See the Terms and Conditions (https://onlinelibrary.wiley.com/terms-and-conditions) on Wiley Online Library for rules of use; OA articles are governed by the applicable Creative Commons License

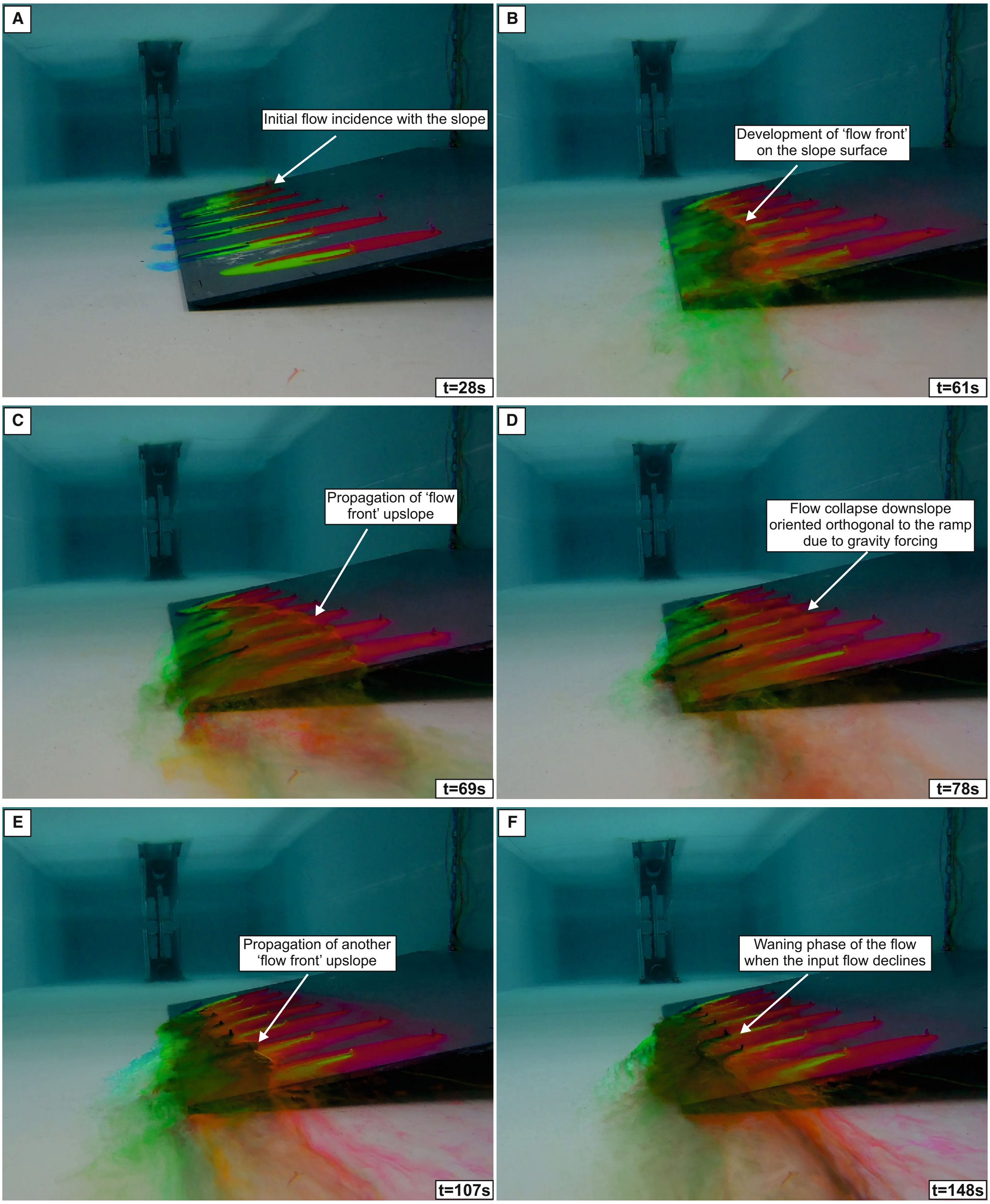

Fig. 18. Example images (A–F) looking upstream depicting the temporal evolution of density currents upon incidence with a flow-parallel topographic slope of 10° slope gradient. *t* denotes the experimental time since the release of the flow from the mixing tank. Dye injection on the slope is used to visualize the flow behaviour. Note the repeated flow-front growth and collapse above the topographic slope moving in an orthogonal direction to the slope, with localized rugosity along the 'flow front' (also see Video 5 for more detail of this flow behaviour).

13653091, 0, Downloaded from https://onlinelibrary.wiley.com/doi/10.1111/sed.70032 by Schweizerische Akademie Der, Wiley Online Library on [20/07/2025]. See the Terms and Conditions (https://onlinelibrary.wiley.com/terms-and-conditions) on Wiley Online Library for rules of use; OA articles are governed by the applicable Creative Commons License

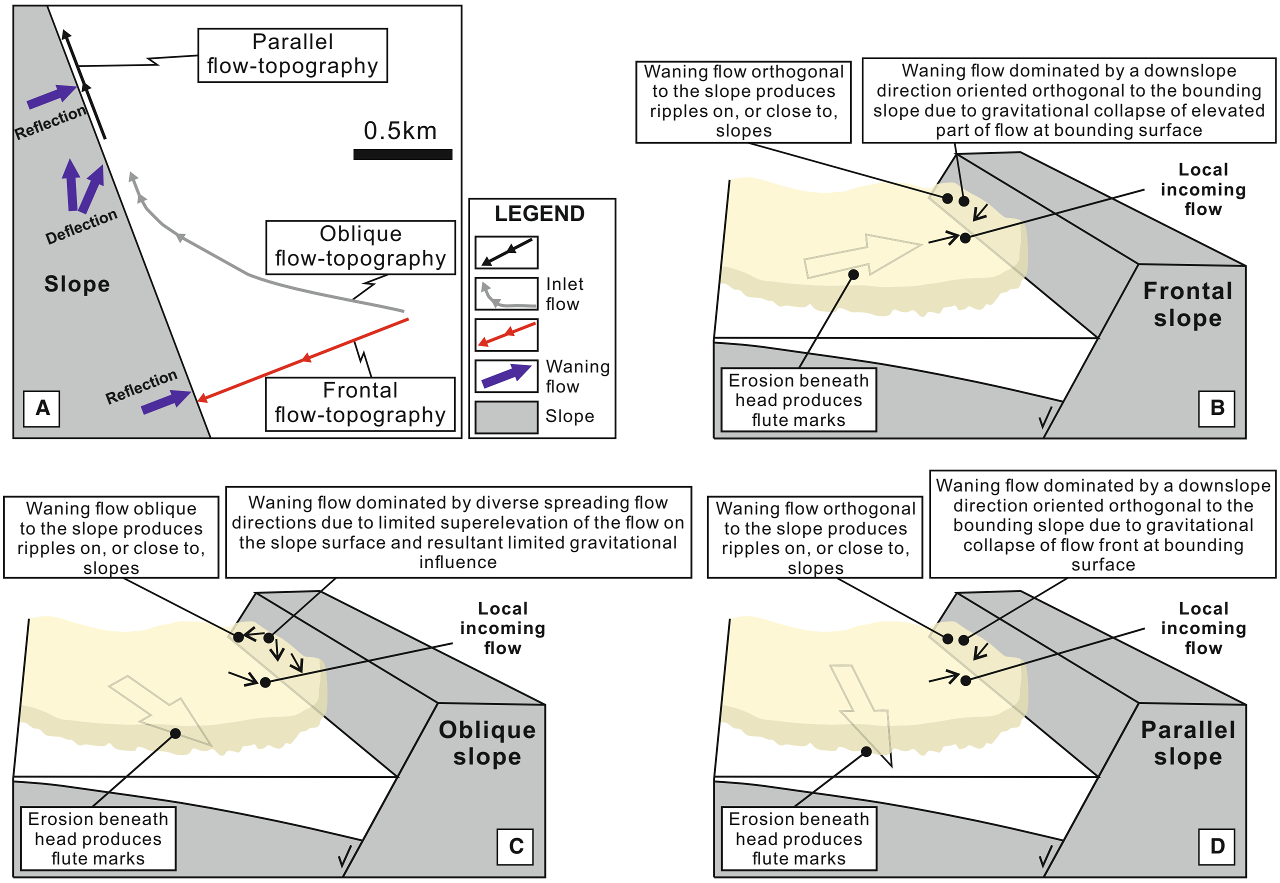

Fig. 19. A new process model proposed in this work highlighting the importance of the incidence angle of the flow against the slope on flow reflection and deflection, presented in a plan view (A) and perspective views (B–D), respectively. Flows that are at very high angles to topographic slopes (A and B) produce orthogonal reflections down the slope. As flows become more oblique (A and C), they are deflected rather than reflected, and do not exhibit orthogonal reflections, even in the case of waning flows that might be expected to generate ripples. Once flows become parallel or broadly parallel to topographic slopes (incidence angle of 0°; A and D), however, they exhibit flow-front growth and collapse on their flank against the bounding topographic slope. The collapsing flows on the flank thus are driven purely by gravity and show orthogonal flow directions relative to the slope. In B–D, ripples are formed on slopes and close to the base of slopes by flows moving down the slope, in many cases during the waning of flows, rather than being the product of internal waves travelling on the upper interface of the gravity current, as shown in Fig. 17B.

further consideration is that flow concentration will change rapidly both spatially and temporally as a result of erosion and sedimentation, and this will influence the flow dynamics. For instance, the downslope collapse might be expected to be less pronounced if sedimentation occurs upslope, due to reduced downslope driving force. Additionally, gentler topographic slopes are common in many deep-water basins (e.g. Bakke *et al.*, 2013; Spychala *et al.*, 2017). Interaction of turbidity currents with lower angle slopes, <20°, is likely to result in more enhanced superelevation of gravity currents running up on the slope surface, more prominent flow decoupling and flow divergence and the generation of highly multidirectional combined flows on slopes. The enhancement in the degree and areal coverage of multidirectional flow on these lower angle slopes is postulated to further limit the inception of trains of internal waves. In terms of sedimentation, the changes in flow on lower slopes may lead to the formation of more isotropic hummock-like bedforms (Keavney *et al.*, 2025).

CONCLUSIONS

This study presents large-scale 3D physical experiments of unconfined gravity currents

© 2025 The Author(s). *Sedimentology* published by John Wiley & Sons Ltd on behalf of
International Association of Sedimentologists, *Sedimentology*

13653091, 0, Downloaded from https://onlinelibrary.wiley.com/doi/10.1111/sed.70032 by Schweizerische Akademie Der, Wiley Online Library on [20/07/2025]. See the Terms and Conditions (https://onlinelibrary.wiley.com/terms-and-conditions) on Wiley Online Library for rules of use; OA articles are governed by the applicable Creative Commons License

interacting with planar slopes of varying orientations and gradients. Results demonstrate a transition in dominant flow processes from divergence- through reflection- to deflection-dominated as the flow incidence angle decreases from 90° to 15° and the slope gradient increases from 20° to 40°. Variability in near-bed velocity pulsing patterns at the base and on the slope is shown to correlate with both flow incidence angle and slope gradient. In all ramp experiments, complex multidirectional combined flows are observed on and at the base of slopes, the unidirectional component of which is a function of the location on a single slope, the incidence angle of the flow relative to the slope and the slope gradient. The observations of multidirectional flows on oblique slopes reinforce the model of Keavney *et al.* (2025) for combined-flow bedforms (such as hummock-like bedforms and sigmoidal bedforms) in the absence of an oscillatory component. This model of combined flow bedforms is extended here, based on the spatial patterns of flow across slopes, and in particular the strength of the unidirectional component, which influences the degree of bedform anisotropy.

Herein, it is demonstrated that the existing model of flow deflection and reflection for planar topographic slopes—where there is a reflected component that is always orthogonal to the slope—which has stood for over three decades, is not supported. Furthermore, the existing model suggests these orthogonal flows are associated with prominent internal waves; however, no evidence of internal waves is found in the present experiments. This absence is attributed to lower density and lower Froude number currents than previous experiments, which are more analogous to natural flows. These develop multidirectional spatially and temporally variable flows on the slope that act against the development of coherent, two-dimensional internal waves. The explanations for ripples at or approaching orthogonal angles to basal sole marks observed in many basin-fills are instead related to transverse motions on flows that are broadly parallel to slopes. These transverse oscillations are produced by changes in flow height or local flow divergence caused by changes to slope orientations, and lead to orthogonal flows relative to the axial sole structures. These aspects are integrated into a new process model of flow interaction with planar slopes.

ACKNOWLEDGEMENTS

This research forms a part of the LOBE 3 consortium project, based at the University of Leeds and the University of Manchester. The authors thank the sponsors of the LOBE 3 consortium project for financial support: Aker BP, BHP, BP, Equinor, HESS, Neptune, Petrobras, PetroChina, Total, Vår Energi and Woodside. Associate Editor Dr Lawrence Amy, Prof. Peter Haughton and two anonymous reviewers are thanked for their constructive comments, which have substantially improved the article.

NOMENCLATURE

H_{max} = Maximum run-upheight (m)
h = Flow height (m)
Fr = Froude number
Fr_d = Densimetric Froude number
g = Acceleration due to gravity (m s^{-2})
g' = Reduced gravitational acceleration (m s^{-2})
h_p = Height of the maximum downstream velocity above the basin floor (m)
Re = Reynolds number
t = Time since the release of the flow from the mixing tank (s)
U = Mean depth-averaged downstream velocity (m s^{-1})
U_{max} = Maximum velocity over height on the time series profiles of longitudinal velocity (m s^{-1})
u = Downstream velocity or longitudinal velocity (m s^{-1})
u_p = Maximum downstream velocity (m s^{-1})
v = Cross-stream velocity or along-slope (strike) velocity (m s^{-1})
w = Vertical velocity (m s^{-1})
μ = Dynamic viscosity(N s m^{-2})
ρ_a = Density of the ambient fluid (kg m^{-3})
ρ_s = Mean depth-averaged density of the current (kg m^{-3})

DATA AVAILABILITY STATEMENT

The data that support the findings of this study are available from the corresponding author upon reasonable request. The high-resolution videos of all the experiments are publicly available and can be downloaded from the Zenodo Repository: https://doi.org/10.5281/zenodo.13988491.

© 2025 The Author(s). *Sedimentology* published by John Wiley & Sons Ltd on behalf of International Association of Sedimentologists, *Sedimentology*

13653091, 0, Downloaded from https://onlinelibrary.wiley.com/doi/10.1111/sed.70032 by Schweizerische Akademie Der, Wiley Online Library on [20/07/2025]. See the Terms and Conditions (https://onlinelibrary.wiley.com/terms-and-conditions) on Wiley Online Library for rules of use; OA articles are governed by the applicable Creative Commons License

REFERENCES

Alexander, J. and **Morris, S.** (1994) Observations on experimental, nonchannelized, high-concentration turbidity currents and variations in deposits around obstacles. *J. Sediment. Res.*, **64**, 899–909.

Allen, C., **Gomis Cartesio, L.E.**, **Hodgson, D.M.**, **Peakall, J.** and **Milana, J.-P.** (2022) Channel incision into a submarine landslide on a Carboniferous basin margin, San Juan, Argentina: evidence for the role of knickpoints. *Depositional Rec.*, **8**, 628–655.

Amy, L.A., **McCaffrey, W.D.** and **Kneller, B.C.** (2004) The influence of a lateral basin-slope on the depositional patterns of natural and experimental turbidity currents. In: *Deep-Water Sedimentation in the Alpine Foreland Basin of SE France: New Perspectives on the Grès d'Annot and Related Systems* (Eds Joseph, P. and Lomas, S.A.), *Geol. Soc. London. Spec. Publ*, **221**, 311–330.

Amy, L.A., **Peakall, J.** and **Talling, P.J.** (2005) Density- and viscosity-stratified gravity currents: insights from laboratory experiments and implications for submarine flow deposits. *Sediment. Geol.*, **179**, 5–29.

Armitage, D.A., **Romans, B.W.**, **Covault, J.A.** and **Graham, S.A.** (2009) The influence of mass-transport-deposit surface topography on the evolution of turbidite architecture: the Sierra Contreras, Tres Pasos Formation (Cretaceous), Southern Chile. *J. Sediment. Res.*, **79**, 287–301.

Ashmore, P.E. (1991a) Channel morphology and bed load pulses in braided, gravel-bed streams. *Geogr. Ann.*, **68**, 361–371.

Ashmore, P.E. (1991b) How do gravel-bed rivers braid? *Can. J. Earth Sci.*, **28**, 326–341.

Athmer, W., **Groenenberg, R.M.**, **Luthi, S.M.**, **Donselaar, M.E.**, **Sokoutis, D.** and **Willingshofer, E.** (2010) Relay ramps as pathways for turbidity currents: a study combining analogue sandbox experiments and numerical flow simulations. *Sedimentology*, **57**, 806–823.

Azpiroz-Zabala, M., **Sumner, E.J.**, **Cartigny, M.J.B.**, **Peakall, J.**, **Clare, M.A.**, **Darby, S.E.**, **Parsons, D.R.**, **Dorrell, R.M.**, **Özsoy, E.**, **Tezcan, D.**, **Wynn, R.B.** and **Johnson, J.** (2024) Benthic biology influences sedimentation in submarine channel bends: coupling of biology, sedimentation and flow. *Deposit. Rec.*, **10**, 159–175.

Baas, J.H., **Tracey, N.D.** and **Peakall, J.** (2021) Sole marks reveal deep-marine depositional process and environment: implications for flow transformation and hybrid event bed models. *J. Sediment. Res.*, **91**, 986–1009.

Baines, P.G. (1995) *Topographic Effects in Stratified Flows*, p. 482. Cambridge University Press Monographs on Mechanics, Cambridge, UK.

Bakke, K., **Kane, I.A.**, **Martinsen, O.J.**, **Petersen, S.A.**, **Johansen, T.A.**, **Hustoft, S.**, **Jacobsen, F.H.** and **Groth, A.** (2013) Seismic modeling in the analysis of deep-water sandstone termination styles. *AAPG Bull.*, **97**, 1395–1419.

Baudouy, L., **Haughton, P.D.** and **Walsh, J.J.** (2021) Evolution of a fault-controlled, deep-water Sub-Basin, Tabernas, SE Spain. *Front. Earth Sci.*, **9**, 767286.

Bell, D., **Stevenson, C.J.**, **Kane, I.A.**, **Hodgson, D.M.** and **Poyatos-Moré, M.** (2018) Topographic controls on the development of contemporaneous but contrasting basin-floor depositional architectures. *J. Sediment. Res.*, **88**, 1166–1189.

Best, J.L., **Kirkbride, A.D.** and **Peakall, J.** (2001) Mean flow and turbulence structure of sediment-laden gravity currents: new insights using ultrasonic Doppler velocity profiling. In: *Particulate Gravity Currents* (Eds McCaffrey, W.D., Kneller, B.C. and Peakall, J.), *IAS Spec. Publ*, **31**, 159–172.

Best, J.L., **Kostaschuk, R.A.**, **Peakall, J.**, **Villard, P.V.** and **Franklin, M.** (2005) Whole flow field dynamics and velocity pulsing within natural sediment-laden underflows. *Geology*, **33**, 765–768.

Brunt, R.L., **McCaffrey, W.D.** and **Kneller, B.C.** (2004) Experimental modelling of the spatial distribution of grain size developed in a fill-and-spill mini-basin setting. *J. Sediment. Res.*, **74**, 438–446.

Bruschi, R., **Bughi, S.**, **Spinazzè, M.**, **Torselletti, E.** and **Vitali, L.** (2006) Impact of debris flows and turbidity currents on seafloor structures. *Norw. J. Geol.*, **86**, 317–336.

Buckee, C., **Kneller, B.** and **Peakall, J.** (2001) Turbulence Structure in Steady, Solute-Driven Gravity Currents. In: *Particulate Gravity Currents* (Eds McCaffrey, W., Kneller, B. and Peakall, J.), *Int. Assoc. Sedimentol. Spec. Pub*, **31**, 173–187.

Carter, L., **Gavey, R.**, **Talling, P.** and **Liu, J.** (2014) Insights into submarine geohazards from breaks in subsea telecommunication cables. *Oceanography*, **27**, 58–67.

Chadwick, R., **Zweigel, P.**, **Gregersen, U.**, **Kirby, G.A.**, **Holloway, S.** and **Johannessen, P.** (2004) Geological reservoir characterization of a CO_2 storage site: the Utsira Sand, Sleipner, Northern North Sea. *Energy*, **29**, 1371–1381.

Cope, R.N. (1959) The Silurian rocks of the Devilsbit Mountain district, County Tipperary. *Proc. Roy. Irish Acad.*, **60**, 217–242.

Craig, G.Y. and **Walton, E.K.** (1962) Sedimentary structures and palaeocurrent directions from the Silurian rocks of Kirkcudbrightshire. *Trans. Edinb. Geol. Soc.*, **19**, 100–119.

Cullen, T.M., **Collier, R.E.L.**, **Gawthorpe, R.L.**, **Hodgson, D.M.** and **Barrett, B.J.** (2020) Axial and transverse deep-water sediment supply to syn-rift fault terraces: insights from the West Xylokastro Fault Block, Gulf of Corinth, Greece. *Basin Res.*, **32**, 1105–1139.

Cumberpatch, Z.A., **Kane, I.A.**, **Soutter, E.L.**, **Hodgson, D.M.**, **Jackson, C.A.-L.**, **Kilhams, B.A.** and **Poprawski, Y.** (2021) Interactions between deep-water gravity flows and active salt tectonics. *J. Sediment. Res.*, **91**, 34–65.

Dai, A. (2008) *Analysis and modeling of plunging flows*. PhD thesis. University of Illinois at Urbana-Champaign, Urbana-Champaign, IL.

Dorrell, R.M., **Darby, S.E.**, **Peakall, J.**, **Sumner, E.S.**, **Parsons, D.R.** and **Wynn, R.B.** (2014) The critical role of stratification in submarine channels: implications for channelization and long run-out flows. *J. Geophys. Res. Oceans*, **119**, 2620–2641.

Dorrell, R.M., **Peakall, J.**, **Sumner, E.J.**, **Parsons, D.R.**, **Darby, S.E.**, **Wynn, R.B.**, **Özsoy, E.** and **Tezcan, D.** (2016) Flow dynamics and mixing processes in hydraulic jump arrays: implications for channel-lobe transition zones. *Mar. Geol.*, **381**, 181–193.

Dorrell, R.M., **Peakall, J.**, **Burns, C.** and **Keevil, G.M.** (2018) A novel mechanism in sinuous seafloor channels: implications for submarine channel evolution. *Geomorphology*, **303**, 1–12.

Dorrell, R.M., **Peakall, J.**, **Darby, S.E.**, **Parsons, D.R.**, **Johnson, J.**, **Sumner, E.J.**, **Wynn, R.B.**, **Özsoy, E.** and **Tezcan, D.** (2019) Self-sharpening induces jet-like structure in seafloor gravity currents. *Nat. Commun.*, **10**, 1381.

Dzulynski, S., **Ksiazkiewicz, M.** and **Kuenen, P.H.** (1959) Turbidites in flysch of the Polish Carpathian Mountains. *Geol. Soc. Am. Bull.*, **70**, 1089–1118.

© 2025 The Author(s). *Sedimentology* published by John Wiley & Sons Ltd on behalf of International Association of Sedimentologists, *Sedimentology*

13653091, 0, Downloaded from https://onlinelibrary.wiley.com/doi/10.1111/sed.70032 by Schweizerische Akademie Der, Wiley Online Library on [20/07/2025]. See the Terms and Conditions (https://onlinelibrary.wiley.com/terms-and-conditions) on Wiley Online Library for rules of use; OA articles are governed by the applicable Creative Commons License

Edwards, D.A., **Leeder, M.R.**, **Best, J.L.** and **Pantin, H.M.** (1994) On experimental reflected density currents and the interpretation of certain turbidites. *Sedimentology*, **41**, 437–461.

Gladstone, C., **Ritchie, L.J.**, **Sparks, S.J.** and **Woods, A.W.** (2004) An experimental investigation of density-stratified inertial gravity currents. *Sedimentology*, **51**, 767–789.

Graf, W.H. (1971) *Hydraulics of Sediment Transport*, p. 513. McGraw Hill, New York, NY.

Haughton, P.D. (1994) Deposits of deflected and ponded turbidity currents, Sorbas Basin, Southeast Spain. *J. Sediment. Res.*, **64**, 233–246.

Haughton, P.D. (2000) Evolving turbidite systems on a deforming basin floor, Tabernas, SE Spain. *Sedimentology*, **47**, 497–518.

Haward, M. (2018) Plastic pollution of the world's seas and oceans as a contemporary challenge in ocean governance. *Nat. Commun.*, **9**, 667.

Hill, P.R. and **Lintern, D.G.** (2022) Turbidity currents on the open slope of the Fraser Delta. *Mar. Geol.*, **445**, 106738.

Hilton, V. and **Pickering, K.T.** (1998) *Turbidite Systems of Southeast France*, p. 229. Vallis Press, London.

Ho, V.L., **Dorrell, R.M.**, **Keevil, G.M.**, **Thomas, R.E.**, **Burns, A.D.**, **Baas, J.H.** and **McCaffrey, W.D.** (2019) Dynamics and deposition of sediment-bearing multi-pulsed flows and geological implication. *J. Sediment. Res.*, **89**, 1127–1139.

Hodgson, D.M. and **Haughton, P.D.** (2004) Impact of syndepositional faulting on gravity current behaviour and deep-water stratigraphy: Tabernas-Sorbas Basin, SE Spain. In: *Confined Turbidite Systems* (Eds Lomas, S.A. and Joseph, P.), *Geol. Soc. Spec. Publ*, **222**, 135–158.

Hofstra, M., **Peakall, J.**, **Hodgson, D.M.** and **Stevenson, C.J.** (2018) Architecture and morphodynamics of subcritical sediment waves in ancient channel-lobe transition zone. *Sedimentology*, **65**, 2339–2367.

Howlett, D.M., **Ge, Z.**, **Nemec, W.**, **Gawthorpe, R.L.**, **Rotevatn, A.** and **Jackson, C.A.-L.** (2019) Response of unconfined turbidity currents to deep-water fold and thrust belt topography: orthogonal incidence on solitary and segmented folds. *Sedimentology*, **66**, 2425–2454.

Howlett, D.M., **Gawthorpe, R.L.**, **Ge, Z.**, **Rotevatn, A.** and **Jackson, C.A.-L.** (2021) Turbidites, topography and tectonics: evolution of submarine channel-lobe systems in the salt-influenced Kwanza Basin, offshore Angola. *Basin Res.*, **33**, 1076–1110.

Huang, H., **Imran, J.**, **Pirmez, C.**, **Zhang, Q.** and **Chen, G.** (2009) The critical densimetric Froude number of subaqueous gravity currents can be non-unity or non-existent. *J. Sediment. Res.*, **79**, 479–485.

Joseph, P., **Babonneau, N.**, **Bourgeois, A.**, **Cotteret, G.**, **Eschard, R.**, **Garin, B.**, **Granjeon, D.**, **Lerat, O.**, **Ravenee, C.**, **Domes de Souza, O.**, **Guillocheau, F.** and **Qemener, J.M.** (2000) The Annot sandstone outcrops (Franch Alps): architecture description as input for quantification and 3D reservoir modeling. In: *Deep-Water Reservoirs of the World* (Eds Weimer, P., Slatt, R.M., Coleman, J., Rosen, N.C., Nelson, H., Bouma, A.H., Styzen, M.J. and Lawrence, D.T.), pp. 422–449. SEPM Society for Sedimentary Geology, Tulsa, OK.

Kane, I.A., **Clare, M.A.**, **Miramontes, E.**, **Wogelius, R.**, **Rothwell, J.J.**, **Garreau, P.** and **Pohl, F.** (2020) Seafloor microplastic hotspots controlled by deep-sea circulation. *Science*, **368**, 1140–1145.

Keavney, E., **Peakall, J.**, **Wang, R.**, **Hodgson, D.M.**, **Kane, I.A.**, **Keevil, G.M.**, **Brown, H.C.**, **Clare, M.A.** and **Hughes, M.** (2025) Unconfined gravity current interactions with orthogonal topography: implications for combined-flow processes and the depositional record. *Sedimentology*, **72**, 67–99.

Keevil, G.M., **Peakall, J.**, **Best, J.L.** and **Amos, K.J.** (2006) Flow structure in sinuous submarine channels: velocity and turbulence structure of an experimental submarine channel. *Mar. Geol.*, **229**, 241–257.

Kelling, G. (1964) The turbidite concept in Britain. In: *Turbidites (Developments in Sedimentology)* (Eds Bouma, A.H. and Brouwer, A.), pp. 75–92. Elsevier, Amsterdam.

Kneller, B. (1995) Beyond the Turbidite Paradigm: Physical Models for Deposition of Turbidites and their Implications for Reservoir Prediction. In: *Characterisation of Deep Marine Clastic Systems* (Eds Hartley, A.J. and Prosser, D.J.), *Geol. Soc. London. Spec. Publ*, **94**, pp. 31–49.

Kneller, B. and **Buckee, C.** (2000) The structure and fluid mechanics of turbidity currents: a review of some recent studies and their geological implications. *Sedimentology*, **47**, 62–94.

Kneller, B.C. and **McCaffrey, W.D.** (1995) Modelling the Effects of Salt-Induced Topography on Deposition from Turbidity Currents. In: *Salt, Sediment and Hydrocarbons: Gulf Coast Society of Economic Paleontologists and Mineralogists Foundation Sixteenth Annual Research Conference 1995* (Eds Travis, C.J., Vendeville, B.C., Harrison, H., Peel, F.J., Hudec, M.R. and Perkins, B.E.), pp. 137–145. SEPM Society for Sedimentary Geology, Tulsa, OK.

Kneller, B. and **McCaffrey, W.** (1999) Depositional effects of flow nonuniformity and stratification within turbidity currents approaching a bounding slope: deflection, reflection, and facies variation. *J. Sediment. Res.*, **69**, 980–991.

Kneller, B., **Edwards, D.**, **McCaffrey, W.** and **Moore, R.** (1991) Oblique reflection of turbidity currents. *Geology*, **14**, 250–252.

Kneller, B.C., **Bennett, S.J.** and **McCaffrey, W.D.** (1997) Velocity and turbulence structure of density currents and internal solitary waves: potential sediment transport and the formation of wave ripples in deep water. *Sediment. Geol.*, **112**, 235–250.

Komar, P.D. (1972) Relative significance of head and body spill from a channelized turbidity current. *Geol. Soc. Am. Bull.*, **83**, 1151–1156.

Konsoer, K., **Zinger, J.** and **Parker, G.** (2013) Bankfull hydraulic geometry of submarine channels created by turbidity currents: relations between bankfull channel characteristics and formative flow discharge. *J. Geophys. Res. Earth*, **118**, 216–228.

Kostaschuk, R., **Nasr-Azadani, M.M.**, **Meiburg, E.**, **Wei, T.**, **Chen, Z.**, **Negretti, M.E.**, **Best, J.**, **Peakall, J.** and **Parsons, D.R.** (2018) On the causes of pulsing in continuous turbidity currents. *J. Geophys. Res. Earth Surf.*, **123**, 2827–2843.

Kuenen, P.H. and **Migliorini, C.I.** (1950) Turbidity currents as a cause of graded bedding. *J. Geol.*, **58**, 91–127.

Li, G., **Tang, Z.**, **Yue, S.**, **Zhuang, K.** and **Wei, H.** (2001) Sedimentation in the shear front off the Yellow River mouth. *Cont. Shelf Res.*, **21**, 607–625.

Lintern, D.G., **Hill, P.R.** and **Stacey, C.** (2016) Powerful unconfined turbidity current captured by cabled observatory on the Fraser River delta slope, British Columbia, Canada. *Sedimentology*, **63**, 1041–1064.

Lloyd, C., **Huuse, M.**, **Barrett, B.J.** and **Newton, A.M.W.** (2021) Regional exploration and characterisation of CO_2 storage prospects in the Utsira-Skade aquifer, North Viking graben, North Sea. *Earth Sci. Syst. Soc.*, **1**, 10041.

13653091, 0, Downloaded from https://onlinelibrary.wiley.com/doi/10.1111/sed.70032 by Schweizerische Akademie Der, Wiley Online Library on [20/07/2025]. See the Terms and Conditions (https://onlinelibrary.wiley.com/terms-and-conditions) on Wiley Online Library for rules of use; OA articles are governed by the applicable Creative Commons License

Lloyd, C.J., **Dorrell, R.M.** and **Caulifield, C.P.** (2022) The coupled dynamics of internal waves and hairpin vortices in stratified plane Poiseuille flow. *J. Fluid Mech.*, **934**, A10.

Lomas, S.A. and **Joseph, P.** (2004) Confined Turbidite Systems. In: *Confined Turbidite Systems* (Eds Lomas, S.A. and Joseph, P.), *Geol. Soc. Spec. Publ*, **222**, 1–7.

Lusseyran, F., **Izrar, B.**, **Audemar, C.** and **Skali-lami, S.** (2003) Time-space characteristics of stratified shear layer from UVP measurements. *Exp. Fluids*, **35**, 32–40.

Marjanac, T. (1990) Reflected sediment gravity flows and their deposits in flysch of Middle Dalmatia, Yugoslavia. *Sedimentology*, **37**, 921–929.

Marshall, C.R., **Dorrell, R.M.**, **Keevil, G.M.**, **Peakall, J.** and **Tobias, S.M.** (2021) Observations of large-scale coherent structures in gravity currents: implications for flow dynamics. *Exp. Fluids*, **62**, 120.

Marshall, C.R., **Dorrell, R.M.**, **Keevil, G.M.**, **Peakall, J.** and **Tobias, S.M.** (2023) On the role of transverse motion in pseudo-steady gravity currents. *Exp. Fluids*, **64**, 63.

Martínez-Doñate, A., **Privat, A.M.-L.**, **Hodgson, D.M.**, **Jackson, C.A.-L.**, **Kane, I.A.**, **Spychala, Y.T.**, **Duller, R.A.**, **Stevenson, C.**, **Keavney, E.**, **Schwarz, E.** and **Flint, S.S.** (2021) Substrate entrainment, depositional relief, and sediment capture: impact of a submarine landslide on flow process and sediment supply. *Front. Earth Sci.*, **9**, 757617.

McCaffrey, W.D. and **Kneller, B.C.** (2001) Process controls on the development of stratigraphic trap potential on the margins of confined turbidite systems and aids to reservoir evaluation. *AAPG Bull.*, **85**, 971–988.

Menard, H.W. and **Ludwick, J.C.** (1951) Applications of hydraulics to the study of marine turbidity currents. In: *Turbidity Currents and the Transportation of Coarse Sediments to Deep Water* (Ed. Hough, J.L.), pp. 2–13. SEPM Society for Sedimentary Geology, Tulsa, OK.

Muck, M.T. and **Underwood, M.B.** (1990) Upslope flow of turbidity currents: a comparison among field observations, theory, and laboratory methods. *Geology*, **18**, 54–57.

Mulder, T., **Razin, P.** and **Faugeres, J.-C.** (2009) Hummocky cross-stratification-like structures in deep-sea turbidites: upper Cretaceous Basque basins (Western Pyrenees, France). *Sedimentology*, **56**, 997–1015.

Normark, W.R., **Posamentier, H.** and **Mutti, E.** (1993) Turbidite systems: state of the art and future directions. *Rev. Geophys.*, **31**, 91–116.

Ogston, A.S. and **Sternberg, R.W.** (1999) Sediment-transport events on the northern California continental shelf. *Mar. Geol.*, **154**, 69–82.

Ogston, A.S., **Cacchione, D.A.**, **Sternberg, A.S.** and **Kineke, G.C.** (2000) Observations of storm and river flood-driven sediment transport on the northern California continental shelf. *Cont. Shelf Res.*, **20**, 2141–2162.

Pantin, H.M. and **Leeder, M.R.** (1987) Reverse flow in turbidity currents: the role of internal solitons. *Sedimentology*, **34**, 1143–1155.

Patacci, M., **Haughton, P.D.W.** and **McCaffrey, W.D.** (2015) Flow behaviour of ponded turbidity currents. *J. Sediment. Res.*, **85**, 885–902.

Peakall, J. and **Sumner, E.J.** (2015) Submarine channel flow processes and deposits: a process-product perspective. *Geomorphology*, **244**, 95–120.

Peakall, J., **Ashworth, P.** and **Best, J.** (1996) Physical modelling in fluvial geomorphology: principles, applications and unresolved issues. In: *The Scientific Nature of Geomorphology: Proceedings of the 27th Binghamton Symposium, September 27–29, 1996* (Eds Rhoads, B. and Thorn, C.), pp. 221–253. Wiley and Sons Ltd, Hoboken, NJ.

Peakall, J., **Best, J.L.**, **Baas, J.**, **Hodgson, D.M.**, **Clare, M.A.**, **Talling, P.J.**, **Dorrell, R.M.** and **Lee, D.R.** (2020) An integrated process-based model of flutes and tool marks in deep-water environments: implications for palaeohydraulics, the Bouma sequence, and hybrid event beds. *Sedimentology*, **67**, 1601–1666.

Pickering, K.T. and **Hiscott, R.H.** (1985) Contained (reflected) turbidity currents from the Middle Ordovician Cloridorme Formation, Quebec, Canada: an alternative to the antidune hypothesis. *Sedimentology*, **32**, 373–394.

Pickering, K.T., **Underwood, M.B.** and **Taira, A.** (1992) Open-ocean to trench turbidity-current flow in the Nankai Trough: flow collapse and reflection. *Geology*, **20**, 1099–1102.

Prentice, J.E. (1962) Some aspects of the Variscan fold belt. In: *The Sedimentary History of the Carboniferous in Devon* (Ed. Coe, K.), pp. 93–108. Manchester University Press, Manchester.

Privat, A.M.-L.J., **Hodgson, D.M.**, **Jackson, C.A.-L.**, **Schwarz, E.** and **Peakall, J.** (2021) Evolution from syn-rift carbonates to early post-rift deep-marine intraslope lobes: the role of rift basin physiography on sedimentation patterns. *Sedimentology*, **68**, 2563–2605.

Puigdefàbregas, C., **Gjelberg, J.M.** and **Vaksdal, M.** (2004) The Grès d'annot in the annot syncline: outer basin-margin onlap and associated soft-sediment deformation. In: *Deep-Water Sedimentation in the Alpine Foreland Basin of SE France: New Perspectives on the Grès d'Annot and Related Systems* (Eds Joseph, P. and Lomas, S.A.), *Geol. Soc. London. Spec. Publ*, **221**, 367–388.

Ravnås, R. and **Steel, R.J.** (1997) Contrasting styles of Late Jurassic syn-rift turbidite sedimentation: a comparative study of the Magnus and Oseberg areas, northern North Sea. *Mar. Pet. Geol.*, **14**, 417–449.

Reece, J.K., **Dorrell, R.M.** and **Straub, K.M.** (2024) Circulation of hydraulically ponded turbidity currents and the filling of continental slope minibasins. *Nat. Commun.*, **15**, 2075.

Reece, J.K., **Dorrell, R.M.** and **Straub, K.M.** (2025) Influence of flow discharge and minibasin shape on the flow behavior and depositional mechanics of ponded turbidity currents. *GSA Bulletin*, **137**, 1797–1814.

Remacha, E., **Fernandez, L.P.** and **Maestro, E.** (2005) The transition between sheet-like lobe and basin-plain turbidites in the Hecho Basin (South-Central Pyrenees, Spain). *J. Sediment. Res.*, **75**, 798–819.

Scott, K.M. (1967) Intra-bed palaeocurrent variations in a Silurian flysch sequence, Kircudbrightshire, Southern Uplands of Scotland. *Scott. J. Geol.*, **3**, 268–281.

Seabrook, S., **Mackay, K.**, **Watson, S.J.**, **Clare, M.A.**, **Hunt, J.E.**, **Yeo, I.A.**, **Lane, E.M.**, **Clark, M.R.**, **Wysoczanski, R.**, **Rowden, A.A.**, **Kula, T.**, **Hoffmann, L.J.**, **Armstrong, E.** and **Williams, M.J.M.** (2023) Volcaniclastic density currents explain widespread and diverse seafloor impacts of the 2022 Hunga Volcano eruption. *Nat. Commun.*, **14**, 7881.

Seilacher, A. and **Meischner, D.** (1965) Fazies-analyse im palaozoikum des Oslo-Gebeites. *Geol. Rundsch.*, **54**, 596–619.

Sequeiros, O.E., **Spinewine, B.**, **Beaubouef, R.T.**, **Sun, T.**, **Garcia, M.H.** and **Parker, G.** (2010) Bedload transport and bed resistance associated with density and turbidity currents. *Sedimentology*, **57**, 1463–1490.

Sestini, G. (1970) Flysch facies and turbidite sedimentology. *Sediment. Geol.*, **4**, 559–597.

© 2025 The Author(s). *Sedimentology* published by John Wiley & Sons Ltd on behalf of International Association of Sedimentologists, *Sedimentology*

13653091, 0, Downloaded from https://onlinelibrary.wiley.com/doi/10.1111/sed.70032 by Schweizerische Akademie Der, Wiley Online Library on [20/07/2025]. See the Terms and Conditions (https://onlinelibrary.wiley.com/terms-and-conditions) on Wiley Online Library for rules of use; OA articles are governed by the applicable Creative Commons License

Simmons, S.M., **Azpiroz-Zabala, M.**, **Cartigny, M.J.B.**, **Clare, M.A.**, **Cooper, C.**, **Parsons, D.R.**, **Pope, E.L.**, **Sumner, E.J.** and **Talling, P.J.** (2020) Novel acoustic method provides first detailed measurements of sediment concentration structure within submarine turbidity currents. *J. Geophys. Res. Oceans*, **125**, e2019JC015904.

Sinclair, H.D. (1994) The influence of lateral basinal slopes on turbidite sedimentation in the Annot Sandstones of SE France. *J. Sediment. Res.*, **64**, 42–54.

Smith, R.D.A. and **Anketell, J.M.** (1992) Welsh Basin 'contourites' reinterpreted as fine-grained turbidites: the Grogal Sandstones. *Geol. Mag.*, **129**, 609–614.

Smith, R. and **Joseph, P.** (2004) Onlap stratal architectures in the Grès d'Annot: geometric models and controlling factors. In: *Deep-Water Sedimentation in the Alpine Basin of SE France: New Perspectives on the Grès d'Annot and Related Systems* (Eds Joseph, P. and Lomas, S.A.), Vol. **221**, pp. 389–399. Geological Society, Bath.

Southern, S.J., **Patacci, M.**, **Felletti, F.** and **McCaffrey, W.D.** (2015) Influence of flow containment and substrate entrainment upon sandy hybrid event beds containing a co-genetic mud-clast-rich division. *Sediment. Geol.*, **321**, 105–122.

Soutter, E.L., **Kane, I.A.**, **Fuhrmann, A.**, **Cumberpatch, Z.A.** and **Huuse, M.** (2019) The stratigraphic evolution of onlap in siliciclastic deep-water systems: autogenic modulation of allogenic signals. *J. Sediment. Res.*, **89**, 890–917.

Soutter, E.L., **Bell, D.**, **Cumberpatch, Z.A.**, **Ferguson, R.A.**, **Spychala, Y.T.**, **Kane, I.A.** and **Eggenhuisen, J.T.** (2021) The influence of confining topography orientation on experimental turbidity currents and geological implications. *Front. Earth Sci.*, **8**, 540633.

Spychala, Y.T., **Hodgson, D.M.**, **Stevenson, C.J.** and **Flint, S.S.** (2017) Aggradational lobe fringes: the influence of subtle intrabasinal seabed topography on sediment gravity flow processes and lobe stacking patterns. *Sedimentology*, **64**, 582–608.

Stevenson, C.J., **Talling, P.J.**, **Wynn, R.B.**, **Masson, D.G.**, **Hunt, J.E.**, **Frenz, M.**, **Akhmetzhanov, A.** and **Cronin, B.T.** (2013) The flows that left no trace: very large-volume turbidity currents that bypassed sediment through submarine channels without eroding the sea floor. *Mar. Pet. Geol.*, **41**, 186–205.

Sumner, E.J., **Peakall, J.**, **Parsons, D.R.**, **Wynn, R.B.**, **Darby, S.E.**, **Dorrell, R.M.**, **McPhail, S.D.**, **Perrett, J.**, **Webb, A.** and **White, D.** (2013) First direct measurements of hydraulic jumps in an active submarine density current. *Geophys. Res. Lett.*, **40**, 5904–5908.

Sumner, E.J., **Peakall, J.**, **Dorrell, R.M.**, **Parsons, D.R.**, **Darby, S.E.**, **Wynn, R.B.**, **McPhail, S.D.**, **Perrett, J.**, **Webb, A.** and **White, D.** (2014) Driven around the bend: spatial evolution and controls on the orientation of helical bend flow in a natural submarine gravity current. *J. Geophys. Res. Oceans*, **119**, 898–913.

Syvitski, J.P.M. and **Hein, F.J.** (1991) Sedimentology of an Arctic basin: Itirbilung Fiord, Baffin Island, Northwest Territories. *Geological Survey of Canada Paper*, **90**, 66.

Takeda, Y. (1991) Development of an Ultrasound Velocity Profile Monitor. *Nucl. Eng. Des.*, **126**, 277–284.

Takeda, Y. (1993) Velocity profile measurement by Ultrasonic Doppler Method. In: *Experimental Heat Transfer, Fluid Mechanics and Thermodynamics* (Ed. Kelleher, M.D.), pp. 126–131. Elsevier, Amsterdam.

Taylor, W.J., **Hodgson, D.M.**, **Peakall, J.**, **Kane, I.A.**, **Morris, E.A.** and **Flint, S.S.** (2024) Unidirectional and combined transitional flow bedforms: controls on process and distribution in submarine slope settings. *Sedimentology*, **71**, 1329–1362.

Thomas, R.E., **Schindfessel, L.**, **McLelland, S.J.**, **Creëlle, S.** and **De Mulder, T.** (2017) Bias in mean velocities and noise in variances and covariances measured using a multistatic acoustic profiler: the Nortek Vectrino Profiler. *Meas. Sci. Technol.*, **28**, 75302.

Tinterri, R. (2011) Combined flow sedimentary structures and the genetic link between sigmoidal- and hummocky-cross stratification. *Geoacta*, **10**, 43–85.

Tinterri, R. and **Muzzi Magalhaes, P.** (2011) Synsedimentary structural control on foredeep turbidites related to basin segmentation: facies response to the increase in tectonic confinement (Marnoso-arenacea Formation, Miocene, Northern Apennines, Italy). *Mar. Petrol. Geol.*, **67**, 81–110.

Tinterri, R., **Muzzi Magalhaes, P.**, **Tagliaferri, A.** and **Cunha, R.S.** (2016) Convolute laminations and load structures in turbidites as indicators of flow reflections and decelerations against bounding slopes. Examples from the Marnoso-arenacea Formation (northern Italy) and Annot Sandstones (south eastern France). *Sediment. Geol.*, **344**, 382–407.

Tinterri, R., **Mazza, T.** and **Muzzi Magalhaes, P.** (2022) Contained-reflected megaturbidites of the Marnoso-arenacea Formation (Contessa Key Bed) and Helminthoid Flysches (Northern Apennines, Italy) and Hecho Group (South-Western Pyrenees). *Front. Earth Sci.*, **25**, 817012.

Tőkés, L. and **Patacci, M.** (2018) Quantifying tabularity of turbidite beds and its relationship to the inferred degrees of basin confinement. *Mar. Pet. Geol.*, **97**, 659–671.

Tomasso, M. and **Sinclair, H.D.** (2004) Deep-water sedimentation of an evolving fault-block: the Braux and St Benoit outcrops of the Grès d'Annot. In: *Deep-Water Sedimentation in the Alpine Basin of SE France: New Perspectives on the Grès d'Annot and Related Systems* (Eds Joseph, P. and Lomas, S.A.), Vol. **221**, pp. 267–283. Geological Society, Bath.

Toniolo, H., **Lamb, M.** and **Parker, G.** (2006) Depositional turbidity currents in diapiric minibasins on the continental slope: formation and theory. *J. Sediment. Res.*, **76**, 783–797.

Wei, T., **Peakall, J.**, **Parsons, D.R.**, **Chen, Z.**, **Zhao, B.** and **Best, J.L.** (2013) Three-dimensional gravity-current flow within a subaqueous bend: spatial evolution and force balance variations. *Sedimentology*, **60**, 1668–1680.

Wright, L.D., **Friedrichs, C.T.** and **Scully, M.E.** (2002) Pulsational gravity-driven sediment transport on two energetic shelves. *Cont. Shelf Res.*, **22**, 2443–2460.

Yalin, M.S. (1971) *Theory of Hydraulic Models*, p. 266. Macmillan, London.

Manuscript received 16 May 2024; revision accepted 2 July 2025

Supporting Information

Additional information may be found in the online version of this article:

Data S1. Supporting Information 1: Derivation of the input parameters for the estimation of the Flow Reynolds number and densimetric Froude number. **Supporting Information 2:** Streamline analysis.

13653091, 0, Downloaded from https://onlinelibrary.wiley.com/doi/10.1111/sed.70032 by Schweizerische Akademie Der, Wiley Online Library on [20/07/2025]. See the Terms and Conditions (https://onlinelibrary.wiley.com/terms-and-conditions) on Wiley Online Library for rules of use; OA articles are governed by the applicable Creative Commons License

Table S1. Set-up parameters for the Ultrasonic Velocity Profiler (UVP) and Acoustic Doppler Velocimeter (ADV).

Fig. S1. (A and B) Plots of velocity streamlines as a function of time for Experiment S20°IN90°. The plots utilise Acoustic Doppler velocity profiler (ADV) instantaneous longitudinal and vertical velocity measurements. The temporal evolution of the position of the maximum longitudinal velocity, Umax, [i.e., the highest absolute value over the measured height range (0.5–3.0 cm) of the ADV profiles] is also shown (red solid lines). This line is smoothed by applying a moving average over a window of 10 points. Note that in the case where Umax resides at the highest elevation of the ADV measurements (0.03 m), this may mean that the Umax of the full current is not captured by the ADV profile. Arrows on the streamlines directed to the right and left indicate flow travelling outbound and returning towards the inlet, respectively. 'bc' denotes the ADV measurements at the base of slope along the channel-basin centreline and 'mc' denotes the ADV measurements at the central flow front position on the slope surface (in the flow direction), respectively (ADV3 in Figure 1). For reference, the corresponding longitudinal velocity time series is also shown as a coloured band above the streamline panels (left); the scale is shown at top right. (C and D) Vertical profiles of the downstream velocity (solid lines) and the maximum measured velocity in any direction (dashed lines) at several representative time steps throughout the experimental run (right); these correspond to the numbered intervals on the left time series panels.

© 2025 The Author(s). *Sedimentology* published by John Wiley & Sons Ltd on behalf of International Association of Sedimentologists, *Sedimentology*

13653091, 0, Downloaded from https://onlinelibrary.wiley.com/doi/10.1111/sed.70032 by Schweizerische Akademie Der, Wiley Online Library on [20/07/2025]. See the Terms and Conditions (https://onlinelibrary.wiley.com/terms-and-conditions) on Wiley Online Library for rules of use; OA articles are governed by the applicable Creative Commons License